nature electronics

Article

https://doi.org/10.1038/s41928-023-01116-6

A physicochemical-sensing electronic skin for stress response monitoring

In the format provided by the authors and unedited

Table of Content

Supplementary Note 1 | Stress, state anxiety, and mental disorders.

Stress is a complex concept that has often been used to capture a wide range of phenomena[1]. For example, the term "stress" has at times been used to refer to life events or experiences that occur to individuals (e.g., the break-up of a romantic relationship, losing one's job) and at other times to refer to the response to these types of experiences. Given these broad ways in which the term "stress" has often been used, there have been calls to increase the specificity with which aspects of stress (e.g., stimulus, response) are defined[1,2]. For the purposes of this paper, we focus on the stress response, defined as occurring when demands placed on an individual exceed his or her resources to manage those demands[3–5]. Stress responses occur across multiple levels and systems, including cognitive, affective, behavioral, and biological processes. The stress response is relevant to a wide range of mental and physical health outcomes, including depression, anxiety disorders, and cardiovascular disease[6]. In contrast to the stress response, a stressor is an exposure (e.g., a stressful event or stimulus) that triggers this response. In the current study, we examined three stressors: the cold pressor test, a virtual reality rhythm game with a social-evaluative component, and vigorous exercise.

As described above, affective processes can comprise the stress response, and we measured state anxiety as a key psychological response to stress. Indeed, anxiety has been defined as the body's prototypical psychological response to the stress[7]. Unlike trait anxiety, which is a relatively stable characteristic and is not context-specific, state anxiety assesses the experience of anxiety in the moment and thus reflects more transitory responses. Assessing state anxiety permitted us to examine current experiences of anxiety that could change in response to the various stressors.

Mental disorder is defined as mental illness conditions including depression, anxiety disorder, psychosis and post-traumatic stress disorder (PTSD)[8]. Mental disorders differ from normal feelings of nervousness or anxiousness and involve excessive, enduring and negative anxiety[9]. They differ from transient fear or anxiety, often stress-induced, by being persistent[10].

Supplementary Note 2 | Selection of biomarkers and their links with stress responses.

The stress response involves a complex biological mechanism within the nervous, endocrine, and immune systems[11,12]. The perception of stress activates the hypothalamic-pituitary-adrenal (HPA) axis and sympathetic adrenal medullary (SAM) axis from the hypothalamus in the brain. Acetylcholine in nerve fibers from both axes will stimulate the adrenal gland, releasing stress hormones (e.g., epinephrine, norepinephrine, and cortisol) into the blood. Acetylcholine can also activate sudomotor neurons connected to sweat glands that release ion-rich fluids. This sympathetic activity can be indirectly measured through the galvanic skin response (GSR) and sweat electrolyte levels[13]. The released stress hormones from the endocrine system will inhibit insulin production, affecting the synthesis of metabolites such as glucose, lactate, and uric acid (UA), as well as narrow arteries, boosting cardiac activities. We list the correlations between the selected biomarkers and stress levels and their mechanisms as follows.

Pulse. The neurotransmitter acetylcholine can cause the stimulation of the nerves connected to the skeletal muscles and muscles involved in cardiovascular and respiratory function, which results in an amplified force output by the skeletal muscles and an escalated pace of both heart and breathing rate[14]. In the cardiovascular system there are β_1, β_2, α_1, and α_2 adrenergic receptors: β_1 adrenergic receptors are expressed in the heart and increases heart rate as well as contractility; β_2 adrenergic receptors are mainly expressed in vascular smooth muscle and skeletal muscle to increase blood perfusion to target organs; α_1, and α_2 adrenergic receptors are expressed in vascular smooth muscle to elicit vasoconstriction[15].

Galvanic skin response (GSR). Activation of SAM axis in a stress event will promote eccrine glands' secretion to generate sweat on the skin[16]. GSR measures skin resistance between two electrodes, and is a crucial vital sign that monitors skin conductance changes from the variation of the ionic permeability of sweat gland membranes generated by the sympathetic activity, which is directly related to stress arousal and cognitive states[17]. Therefore, identification of the phasic component of GSR allows for the quantification of stress[18]. The sweating response related to stress is reported to mainly be concentrated in the hands, wrists, arms and feet where the sweat glands exist densely, which is not directly associated with environmental temperature but with stressors[19].

Skin temperature. Activation of muscle activity as well as the stimulation of eccrine sweat will cause the change in skin temperature, and psychological stress can also affect body temperature. Psychogenic fever has been a common psychosomatic disease for which is not yet fully understood[20]. Note that, in addition to its importance to stress, skin temperature also has an impact on the signals of many biosensors (e.g., enzyme-based sensors), and thus the skin temperature data is often used to perform biosensor calibration.

Glucose. In addition to physical stress response, stress hormones also induce extensive metabolic changes in a living organism[21]. The secretion of epinephrine and norepinephrine from the adrenal gland stimulates glycogenolysis and promotes gluconeogenesis in the liver, which breaks down

glycogen stored in the liver into glucose, and promotes glucose synthesis from non-carbohydrate precursors to enhance the energy necessary for cellular respiration. The stress hormone cortisol will also promote gluconeogenesis and inhibit insulin production to prevent glucose from being stored. Metabolic biomarkers such as glucose have been identified for chronic stress[22], and elevated levels of fasting glucose as well as post loaded glucose have been found in chronic stress that can cause diabetes[23–25]. Increased levels of glucose have been statistically associated with perceived work stress[26], and increase in glucose was also observed in animal models under acute physical and emotional stress[27,28].

Lactate. Muscle and brain exertion during stress transform glucose into lactate as a metabolic product through anaerobic glycolysis. While increased lactate levels can be obtained through long-term muscle exercise in the absence of oxygen[29], it has also been observed recently that lactate plays a significant role at the level of the central nervous system[30,31]. Lactate is an important energy substrate in astrocytes, and the increase in lactate after acute exhaustive exercise are associated with cognitive domains such as working memory and stress[30], in order to serve as a neuromodulator and protect the central nervous system from stress. Previous studies have also shown that elevated lactate can be observed in venous blood after both physical and pure psychosocial stress tests, while the method was invasive with discrete measurement[32–34]. Continuous measurement of sweat lactate after stressors have not been reported.

Uric acid (UA). UA is another endogenous compound that impacts the stress response. UA levels can impact brain regions that underlie stress reactivity and emotion regulation, and therefore directly regulate psychosocial stress and anxiety[35]. Studies have found that elevated UA is associated with daily stress[36], body anxiety[37] and burnout as well[38]. Increased UA is also commonly observed in patients with chronic stress and mental disorders[39–41].

Sodium ions. The central nervous system has been implicated in electrolyte balance and blood pressure regulation as well[42]. Sweat electrolytes such as Na^+ are crucial biomarkers for sweat rate indicators. Sodium concentration is also an indicator of hydration state, which controls acute stress response[43]. An increase in sweat sodium concentration has been reported in exercise-induced stress[44], as well as in mental stress test[45]. Stress may also cause pressure natriuresis, where inadequate increase in urinary sodium excretion in response to stress-induced blood pressure increase occurs[46].

Potassium ions. Na^+-K^+ pump regulation is a crucial mechanism that controls skeletal muscle contractility[47]. Stress hormones such as epinephrine can induce acute hypokalemia in plasma[48]. Potential stress biomarkers also play critical roles in the prognosis and therapy guidance of stress-related diseases and disorders[49], such as obesity[50], inflammatory[51] and cardiovascular diseases[52]. For example, both K^+ and NH_4^+ are known to be correlated with cardiovascular health and fatigue[53,54].

Ammonium ions. Ammonium appears in the blood mainly due to the breakdown of protein[55]. Psychosocial stress can negatively affect liver metabolism and contribute to the worsening progression of hepatic diseases[56], while ammonium is a biomarker since the liver converts ammonia to urea prior to its excretion[57]. Ammonium ions along with lactate have also been reported to accumulate during graded exercise in humans[58].

Supplementary Note 3 | Mechanism of PB-NiHCF based enzymatic biosensors.

Prussian blue (PB) is a highly efficient and selective mediator of hydrogen peroxide. The oxidation of D-(+)-glucose, L-lactate, and UA can be catalyzed by their corresponding enzyme glucose oxidase (GOx), lactate oxidase (LOx), and uricase (UOx), respectively:

$$\text{D-Glucose} + H_2O + O_2 \xrightarrow{GO_x} \text{D-Gluconic Acid} + H_2O_2 \quad (1)$$

$$\text{L-Lactate} + H_2O + O_2 \xrightarrow{LO_x} \text{Pyruvate} + H_2O_2 \quad (2)$$

$$\text{Uric acid} + H_2O + O_2 \xrightarrow{UO_x} \text{Allantoin} + CO_2 + H_2O_2 \quad (3)$$

The H_2O_2 is then reduced by the reduced form of PB, known as Prussian white (PW):

$$Fe_4^{III}[Fe^{II}(CN)_6]_3(PB) + 4e^- + 4K^+ \rightarrow K_4Fe_4^{II}[Fe^{II}(CN)_6]_3(PW) \quad (4)$$

$$K_4Fe_4^{II}[Fe^{II}(CN)_6]_3(PW) + 2H_2O_2 + 4H^+ \rightarrow Fe_4^{III}[Fe^{II}(CN)_6]_3(PB) + 4H_2O + 4K^+ \quad (5)$$

In neutral and alkaline solutions, however, Equation (5) becomes:

$$K_4Fe_4^{II}[Fe^{II}(CN)_6]_3(PW) + 2H_2O_2 \rightarrow Fe_4^{III}[Fe^{II}(CN)_6]_3(PB) + 4OH^- + 4K^+ \quad (6)$$

Conventional PB-based biosensors suffer from poor stability because PB gradually degrades in neutral and alkaline solutions as the hydroxide ions (OH^-), which is a product of H_2O_2 reduction, can break the Fe−(CN)−Fe bond of PB lattice[59]:

$$Fe_4^{III}[Fe^{II}(CN)_6]_3 + 12OH^- \rightarrow 4Fe(OH)_3 + 3[Fe^{II}(CN)_6]^{4-} \quad (7)$$

Therefore, nickel hexacyanoferrate (NiHCF) is introduced, which is catalytically inactive compared with PB (FeHCF) but protects the PB nanoparticles from degradation. Of all typical transitional metals (Fe, Co, Ni, Cu, Zn), their chemical inertness follows by Zn < Fe < Co < Ni < Cu. NiHCF has been reported to be chemically inert and mechanically stable[60]. Both PB and NiHCF belong to the metal hexacyanoferrate group, which share a similar zeolitic crystal structure and thus could form a composite without significant lattice mismatch (**Supplementary Figs. 8** and **9**). Our electrochemical and SEM characterizations of the PB, PB-NiHCF, PB-CoHCF, and PB-CuHCF electrodes further confirmed the high electrochemical stability of the NiHCF (**Supplementary Figs. 5–7 and 10**). Upon cyclic oxidation and reduction of the PB, K^+ ions from the electrolyte solution could incorporate into the interstitial position, while Ni^{2+} ions could substitute nitrogen-coordinated Fe^{3+} ions due to the wide and negatively charged zeolitic channels in the metal hexacyanoferrates crystal lattice, forming substitutional nickel-ion hexacyanoferrate (NiFe-HCF):

$$Fe_4^{III}[Fe^{II}(CN)_6]_3 + (3+3x)K^+ + 3xNi^{2+} + 3e^- \rightarrow 3K_{1+x}Ni_xFe_{1-x}^{III}[Fe^{II}(CN)_6] + 3xFe^{3+} \quad (8)$$

Further deposition will form a thin protective NiHCF layer on the NiFe-HCF surface and cover the PB redox center. While the inertness of nickel may be unfavorable for hydrogen peroxide transduction, the electronegativity of Ni^{2+} ion is lower than that of Fe^{3+}, and nickel substitution would produce an inductive effect to shift electron cloud of Fe-C, raising C-coordinated Fe ions to a more positive valence state and enhancing electrochemical activity as compensation [61]. Hence the PB-NiHCF bilayer retained catalytic activity inherent to conventional PB, while demonstrating excellent long-term stability.

Besides electrochemical inertness of nickel, the substitution of Fe with Ni increases the stability of the PB lattice framework through zero-strain characteristics during ion insertion/extraction processes[62]. During long-term operation, alkali-metal ions/electrolytes will insert into the subcubes of the lattice as the transition-metal ions change oxidation state[63]. Conventional PB suffers from electrolyte ions as the crystal structure can distort from cubic to a less symmetric rhombohedral or monoclinic geometry (**Supplementary Fig. 9**)[62]. The general electrochemical equation for the insertion of an alkali metal ion into PB follows:

$$Fe_4^{III}[Fe^{II}(CN)_6]_3 + 4A^+ + 4e^- \rightarrow A_4Fe_4^{III}[Fe^{II}(CN)_6]_3 \quad (9)$$

where A is the dominant alkali-metal ions in sweat (i.e. Na^+, K^+). The ion and water insertion process may lead to a large volume variation to accommodate structure change, causing the distortion of the PB lattice, thus reducing structural stability. After nickel substitution, studies have found that the ionic radius of ferrocyanide $Fe_4^{III}[Fe^{II}(CN)_6]_3$ decreases from 4.55 Å to 4.32 Å in $Ni[Fe(CN)_6]$[61]. Additionally, of all typical transitional metal ions, a smaller ionic radius is preferred to withstand ion insertion, where Ni^{2+} < Cu^{2+} (0.73 Å) < Co^{2+} (0.745 Å). Therefore, NiHCF was proved the best candidate among the metal hexacyanoferrate group for PB stabilization in our study (**Supplementary Fig. 7**). The reduced lattice constant after Ni substitution could withstand ion and water insertion and reinforce the lattice effectively, suppressing large structure change during the ion migration process. PB-NiHCF has been reported to exhibit a low mechanical strain with small lattice distortion during ion insertion processes[64], indicating high reversibility of rhombohedral-cubic transition and enhanced cycling performance for long-term stability[62].

Supplementary Note 4 | Mechanism of SEBS/PVC/DOS based ion-selective sensors.

Our solid contact ion-selective sensors (SC-ISEs) consist of inkjet-printed carbon and ion-selective membrane (ISM) directly on top. The ISM contains ionophore, lipophilic anionic sites, membrane plastics, and its plasticizer. The target ion (I^+) can reversibly bind to an ion-selective ionophore (L) at the membrane/solution interface in the following process according to the phase-boundary potential model, where (aq) and (m) represent aqueous phase and membrane phase, respectively[65]:

$$I^+(aq) + L(m) \rightleftarrows I^+L(m) \quad (1)$$

I^+ and lipophilic anionic sites R^- (also known as ion-exchangers) could also reversibly transfer across the carbon/membrane interface, so that electrons could flow to the conductive substrate in the local faradaic process[65]. The free flow of lipophilic anionic sites ensures a constant ion activity in the ISM phase. When the target ion concentration changes, such equilibrium at ISM/solution interface will change its potential accordingly following the well-known Nernst equation:

$$E = E_0 - \frac{RT}{F} \ln \frac{[I^+]_{aq}}{[I^+]_{ISM}} \quad (2)$$

, where E_0 is the standard ion transfer potential, R is universal gas constant, T is temperature, F is Faraday constant. The ion-to-electron transduction process is generally realized by either conductive polymers through redox capacitance or functional materials through an electrical double layer capacitance mechanism[65]. Here, the ISMs are directly placed on top of the inkjet carbon without the usage of traditional conductive polymers as SC layers.

The potential drift ΔE at the carbon/ISM interface can be described as follows:

$$\Delta E = \frac{\Delta Q}{C} \quad (3)$$

, where ΔQ is the transported charge and C is the double-layer capacitance. In order to minimize such potential drift and approach the theoretical Nernst limit, it can be seen that capacitance C needs to be sufficiently large. The inkjet carbon nanoparticles we used have a high surface contact area with the ISM, which could form a big double-layer capacitance at the carbon/ISM interface. The cations in the ISM will attract the electrons in the carbon to establish an electrical double layer, and the higher interfacial contact area, the more efficient this ion-to-electron transduction will be. The natural chemical inertness of carbon also enables an unpolarizable interface to provide a stable phase boundary potential at the SC/ISM interface.

The applications of ISEs typically depend on their potential stability. The potential drifts of ISEs can be attributed to a number of factors including irreversible ion-to-electron conversion during a number of charging/discharging cycles, leaching of ionophore into test solutions and ISM properties. For the ISM membrane, a PVC/DOS matrix has been widely used due to its

characteristically faster ion diffusion coefficients on the order of 10^{-8} cm^2 s^{-1}, which facilitates fast ion partitioning between the organic and aqueous phase[66]. However, pure PVC/DOS-based ISEs may suffer leaching of ionophore and other components from the membrane phase into sample solution as a result of a big diffusion coefficient, which could result in a potential drift of ~2 mV h^{-1} over time[67], and thus is unfavorable for long-term daily monitoring. These leached materials could cause potential inflammatory responses for wearable and in vivo applications as well[65]. Previous studies have introduced the addition of silicone rubber or plasticizers with high lipophilicity into the ISM to improve analytical performance and reduce biofouling[68], but the potential drift was still high in their studies. Here, we introduce thermoplastic elastomer styrene-ethylene-butylene-styrene (SEBS) into the ISM with superior reproducibility and stability. The added stretchable SEBS elastomer could significantly improve the mechanical properties, and promoted the adhesion between ISM and underlying electrode without delamination. The SEBS is highly lipophilic, which will suppress the leaching of active components from the membrane. Such hydrophobicity will also inhibit water formation at the SC/ISM interface, which is the main reason for the SC-ISEs drift and failure due to the intrinsic water uptake and diffusion in the polymeric membrane[65]. In addition to increasing mechanical flexibility and preventing water penetration and leaching, the SEBS polymer has a small ion diffusion coefficient and water diffusion coefficient on the order of 10^{-13} cm^2 s^{-1} [69]. Such low diffusion coefficient on the one hand ensures that the ion concentration within the membrane is relatively stable over a dynamically changing medium, but on the other hand may cause a significantly longer conditioning treatment before equilibrium for pure SEBS-based ISM. Mixing SEBS together with the PVC/DOS can retain the fast ion diffusion coefficients of PVC/DOS matrix relatively and only requires pre-conditioning within an hour, while prolonging sensor lifetime significantly with a negligible drift of merely 0.04 mV h^{-1} over time.

Supplementary Note 5 | Significance of differentiating stressors and stressor designs

Distinguishing types of stressors has been recognized as a necessary condition for understanding the complex interrelationships among distinct stress experiences, as well as the collective impacts of stress on mental health[70–72]. The influence of stress type have been known to cause varying physiological processes in medical students[73], caregivers[74], employees[75], children[76], and adolescents[77,78], as well as in animal models[79]. For example, VR has been adopted in stress training programs to decrease levels of perceived stress and negative affect in military personnel[80]. As the virtual environment guides the patient back to the scene of their traumatic event, where the original stressor occurred, studies have shown that reliving the stressor can help treat PTSD in warfighters[81]. In terms of performance, research has found that adults' reactivity to daily stressors depends on the stressor type, emphasizing the importance in identifying different stressor types for characterizing risk factors[71]. For example, the stressor type has been validated as a modifiable risk factor for coping responses and cardiovascular diseases[72,82]. Therefore, identifying the types of stressors, as well as linkages between types of stressors and human adjustment is highly desired and a prerequisite for stress management[70,77,83].

The two-way communication between the major effector systems and the brain exist to provide feedback and avoid over-reactivity[84]. Therefore, the biological system activation not only depend on objective measures of stressors, but also the subjective perceptions of the stressor[84]. According to the two-factor model on emotions, our body first experiences a physiological arousal to a stressor, which the minds interpret as a psychological feeling or emotion. The cognitive appraisal in the two-factor model is situation dependent, and hence relies on the type of stressor the subject experiences. Our model does not predict an individual emotion but the aggregate of multiple emotions in the form of a state anxiety score. The features used to predict state anxiety should contain information about the stressor given the situational dependance, which is why we tested our platform across different activities and demonstrated the capabilities to use our multimodal sensors for activity differentiation as well as anxiety prediction. Note that our limited number of activities do not fully represent all possible cognitive experiences, which requires a population level of human trials beyond the scope of our study. In our designed stressor experiments, we designed three controlled stress studies to monitor and evaluate stress and anxiety levels. Our study selected the following three stressors, cold pressor test (CPT), virtual reality challenge (VR), and vigorous exercise.

CPT is a validated and reliable acute physiological stressor that triggers immediate HPA axis activation without the need for vigorous activities[85]. CPT has been widely used for stress response studies[86–88], and in our CPT study, while we only observe mild changes of these biomarkers, we did not observe much variations in participants' levels of state anxiety on the STAI questionnaire.

VR is attracting a growing research interest due to its seamless integration capabilities for instilling psychological stress and its highly controllable user experience[89–92]. Previous studies have

validated stressful VR environments to generate psychological stress and a stronger emotional response[93–95], while most studies mainly focused on physical markers monitoring, such as GSR, ECG, and EEG[89–91]. For our VR study, the subjects were required to sit on a chair with one hand playing beat saber. While some hand and arm movement are inevitable, our design has minimized the variation caused by physical activities such as exercise.

Exercise and intense physical training have been validated stressors by numerous studies[96–100], which is related with both physiological and psychological stress. Specifically, the ergometric stress test has been adopted as a standard stress test in many instances[98,101,102]. Previous research has pursued potential biomarkers in sweat that are connected with submaximal exercise[103], but the intermittent and invasive collection cannot show the dynamic change of sweat compositions over time. In our exercise design, the subjects performed maximum-load cycling on a stationary exercise bike with strong verbal encouragement. Strength training has been concluded to induce physiological stress[97]. For athletes, military and fireman that have an intense physical training and work, stress may have serious consequences and impact on performance. Screening potential stress biomarkers in sweat has been studied in sports and exercise, while most studies utilize commercial mass spectrometry to attain a discrete profile rather than continuous monitoring[96]. While physical exercise itself may change the levels of biomarkers in the study, high levels of state anxiety (a key psychological response to stress) were observed on the STAI questionnaire due to acute intense exercise. To further classify and evaluate stress response, we designed a ML pipeline accordingly to find the underlying relationship between biomarkers and stress/anxiety levels of participants.

Supplementary Note 6 | Selection of questionnaires.

Our pioneering study aims to introduce and quantify acute stress responses within a very short period of time without causing experimental interruption, and therefore we seek state measures of the stress response to monitor changes with each particular stressor test. We list here six questionnaire candidates that have been commonly used for stress and anxiety measurement. Each questionnaire and their intentions are discussed below:

The Perceived Stress Scale (PSS) is a classic measure of stress perceptions, which consists of 10 items querying whether individuals perceive their lives to be uncontrollable, unpredictable, and overwhelming[104]. However, the questions in this scale ask about average feelings and thoughts during the last month, and thus do not capture the immediate stress responses central to our study.

The Perceived Stress Questionnaire (PSQ) is an instrument for assessing stressful life events and circumstances that tend to trigger or exacerbate disease symptoms[105]. The questionnaire consists of 30 items, asking the subject's general feeling during the last year or two, and is not suitable for momentary stress response assessment in our study.

The Depression Anxiety Stress Scale (DASS) is a self-report instrument for measuring depression, anxiety and stress altogether[106]. The questionnaire consists of 42 items, and queries average feelings in the past week. It is therefore not aligned with the momentary stress response measures required for our study.

The State-Trait Anxiety Inventory (STAI-Y) is a self-report questionnaire that measures state anxiety. The questionnaire consists of two subscales with 20 items each, of which state anxiety scale Y-1 measures the subject's feeling "right now/at this moment", while trait anxiety scale Y-2 asks for the subject's general feeling. The STAI-Y questionnaire was reported to have a high internal consistency coefficient of 0.91−0.93 for college students and working adults[107]. In practice, since stress and state anxiety are closely correlated, a number of stress research papers used STAI-Y questionnaire for the assessment of stress[93,108–112].

The Beck Anxiety Inventory (BAI) is a self-report measure of anxiety[113]. The questionnaire consists of 21 items of common symptoms of anxiety, and asks the level subjects have been bothered by each symptom during the past month. Thus, it does not capture solely acute stress responses, as required in our study.

The Hospital Anxiety and Depression Scale (HADS) is a questionnaire that assesses both anxiety and depression[114]. It is intended for a general medical patient population, and items measure average feelings in the past week. It is therefore not the optimal tool for assessing stress response in our study.

Thus, we selected the STAI-Y1 as our questionnaire in this study to measure state anxiety level—our key psychological response to stress. Our stress study measures the multimodal stress response as a demonstration for CARES platform, and use ML to classify different stress events. We further use ML to quantify the effect of stress on state anxiety level as a demonstration.

Supplementary Note 7 | Role of artificial intelligence in decoding the links between biomarkers and stress

Biomarker discovery typically requires a large-scale research effort, diversified across activities, especially for complex syndromes such as the stress response due to the interactions between multiple hormones and biological systems. Despite the challenges in validating novel biomarkers for anxiety, there has been a growing pressure to investigate these biomarkers' influence on stress-related disorders. During stress induced activities, multiple systems including physiological vital signs as well as multiorgan-metabolic and endocrine systems are involved and intercorrelated[49]. The stress response is a complex biological process which can cause changes in physiological factors, as well as biofluids of many hormones, metabolites and electrolytes. Given the interplay between different potential biomarkers, analyzing a single marker is therefore not enough to understand the complex activity of the autonomic nervous system, and the only way to assess an individual's unique influence on the stress response is to track and compare each potential biomarker simultaneously. In addition, the ability for continuous monitoring the important stress hormones at physiologically relevant levels has not yet been achieved using wearable sensors. A precise understanding of the relationship between the stress response and general health would involve the analysis of different biomarkers together, understanding the relative importance of each marker, as well as exploring new non-invasive multisystem biomarkers[19].

After integrating multiple biomarkers onto a single platform, isolating stress-related trends becomes difficult. It is therefore natural to apply artificial intelligence (AI) to deconvolute the biological mechanism behind different stress responses, and to study the potential correlations between different biomarkers. The multimodal data collected by the CARES platform are high-dimensional and consists of 60,000 s, making traditional statistical approaches inadequate. ML algorithms, however, excel in these circumstances. They can model complex, nonlinear relationships and interactions among variables, thereby helping to better identify and understand the underlying associations between physiological biomarkers and the stress response. ML models are particularly good at making predictions based on patterns in data. If a reliable connection between physiological biomarkers and stress can be identified, ML can help predict stress and state anxiety levels based on a combination of raw biomarkers, and identify the most relevant features (in this case, biomarkers, as shown in **Fig. 4g, i, j**) that contribute to the outcome. While it is an unsolved problem in machine learning and fundamental computer science field regarding the ML model interpretations and explanability[115,116], in our study we adopted ML to derive correlation between these biomarkers and state anxiety levels, where clinical STAI-Y questionnaire is treated as the gold standard for data training.

Supplementary Note 8 | Pulse analysis and feature extraction.

The pulse analysis algorithm was written as an iterative and adaptive model for analyzing arterial pulse in semi-real time (i.e., after each pulse is fully formed). The first step in the process was to filter and separate individual pulses. During the experiment, pulse data was sampled at a sampling frequency of around 0.007 s. For a typical relaxing heart rate between 60 and 100 beats per minute, this yielded approximately 84 to 139 points per pulse respectively. For this sampling frequency, we found that a Savitzky–Golay (SG) filter with length 9 and order 2 was sufficient to remove small noise within the dataset. We opted for an SG filter over a low pass filter at this stage due to the sharp transitions between pulses from the end of the tail wave to the systolic rise. Applying a low-pass filter would cut off some of the data due to the superposition of low and high frequency components. In particular, the low pass filter at this stage would affect the systolic amplitude as well as the systolic rise time – two important features of the pulse. After the SG filter, the pulse data was noisy, but showed clear distinct features in its first derivative for pulse separation.

Individual pulses were isolated based on the slope of their systolic peak. Instead of choosing a constant systolic threshold across the dataset, we utilized an adaptive iterative method for identifying the systolic rise. We opted for an iterative method as the systolic rise can vary due to biological responses (arterial vein tightening) as well as from amplitude drift in the sensors. However, between subsequent pulses (around 1.6 to 2 seconds), these differences do not significantly affect the systolic slope. After identifying one systolic peak, the next peak could be found using two criteria: at least half the systolic slope and 0.33 seconds (180 beats/min) away from the previous systolic peak. The time duration criteria ensured that the dicrotic peak was not accidently labeled as a systolic peak, while not overshooting and missing the next systolic rise. To calculate the initial systolic slope's threshold, the first 1.5 seconds was used as calibration, where the maximum slope was used as the baseline systolic threshold. After the analysis, each dataset was verified for proper pulse separation, and it was noted that all pulses were properly extracted. To discount noise from wire movements and motion artifacts, if two systolic peaks were identified greater than 2 seconds (30 beats/min) apart, then the corresponding pulse interval was removed. After isolating an individual pulse, second round of filtering was applied to remove the remaining noise. An 18 Hz third order low pass filter was applied followed by another SG filter. After filtering, first, second, and third order derivatives were calculated using an SG filter of length 3 order 2. A linear baseline was subtracted from the start to the end of the pulse to remove the remaining background drift. At this point, all pulses and their derivatives were smooth and ready for feature extraction.

To extract features from specific components of the pulse, derivatives instead of commonly-used gaussian decomposition were utilized to differentiate and segment the pulse waveforms (**Supplementary Fig. 35a**). The peaks detected for each pulse waveform were extracted amplitude and time intervals as features for the ML model. Each pulse waveform was first normalized according to their systolic peak intensity amplitude, which yielded stable feature output against

patch variations as well as moderate motion artifacts (**Supplementary Figs. 36** and **37**). In previous attempts, we added an extra processing method using four gaussian decomposition to further isolate each individual systolic, tidal, dicrotic, and tail wave component of the pulse. This method proved to be time costly with high variability between pulses due to multiple optimal gaussian combinations that fit the overall waveform. Furthermore, even with individual optimization of the decomposition, the features obtained through this method were noisier than features extracted from the pulse directly due to small amplitude variations in the fit. From the systolic peak, four consistent points across all waveforms were identified in the following order of appearance: the systolic peak, the maximum slope, the maximum and minimum second derivative. From the tidal wave, two consistent points across all waveforms were identified in the following order of appearance: the tidal peak and the third derivative maximum after the tidal peak. From the dicrotic wave, four consistent points across all waveforms were identified in the following order of appearance: the dicrotic notch, the maximum slope of the dicrotic rise, the dicrotic peak, and the minimum slope after the dicrotic peak. The tail wave was too noisy to extract meaningful features as the wave is not as large and consistent as the others. Each above group formed a reliable and consistent set of points to extracts various attributes about each waveform. Additionally, if any set of points were not found in the correct order, the pulse was not analyzed, offering a criterion for removing noisy data.

Of the points mentioned above, the tidal peak is known to be weak, requiring high sensitivity to properly measure. Moreover, the tidal peak amplitude can fluctuate within a dataset. Correctly identifying the faintest trace of the tidal peak even when the peak is not visually present was a challenge. This challenge was investigated due to the importance of the tidal feature. There are three main ways we identified the tidal peak. All methods look for the tidal wave within a specific section of the pulse, where the start of the tidal region was defined after the systolic peak, and the end of the tidal region was defined as the dicrotic notch. The algorithm attempted to extract the tidal peak using the following three methods in order of attempts: 1) If the tidal peak was large and well-formed then the tidal peak maximum is the zero-crossing of the first derivative in the tidal region. 2) As the tidal amplitude decreases, the extrema will become a saddle point and is identified by the maximum of the first derivative in the tidal region. 3) If no peak is easily identified in the first derivative due to noise, then we take the second derivative zero crossing (i.e., the maximum of the first derivative peak) in the tidal region. It is important to note that all three searching methods refer to the same saddle point but obtain the index through looking at the next derivative. Each method comes with its own level of tolerance for finding the correct saddle point. In practice, the tidal peak is found mainly through the first derivative, sometimes through the second derivative. A visual example of how we found these points is further shown in **Supplementary Fig. 35b**. Pulse feature extraction was validated upon finding consistent and important features for predicting stress response.

Other than pulse signals, all other physicochemical biomarkers were sampled at a sampling frequency of 1 s. After filtering and normalization, these signals themselves served as a feature and directly went through the ML pipeline.

For overall stress and state anxiety level evaluation, due to the intrinsic limitations of stress questionnaires being able to only characterize an overall stress and state anxiety level within a given time period rather than dynamic stress change continuously, we analyzed the stress response event as a whole to mimic questionnaire functionalities. In this circumstance, the original dataset was reduced, and further feature extraction was performed by taking mean signal changes from the moving average (MA) of sensors rather than segmented at each timepoint. Features were extracted from the relaxation and stress region with a simple MA rolling window of 100 s. Simpler linear ML models, including linear regression, SVM, and stochastic gradient descent regressor were evaluated and performed better in terms of R2 score and mean squared error given the reduced dataset (**Supplementary Fig. 40a,b**). With the reduced size of dataset and simple linear models, we also reduced number of features to prevent overfitting by performing a brute force feature selection within each biomarker (**Supplementary Fig. 40c**). We found that combination of physicochemical features outperformed that of physical and chemical sensors alone, and chemical information can supplement pulse data that we are missing to produce a higher accuracy than either sensor in isolation, allowing us to reduce the feature numbers to four while maintaining a high R^2 score of 91.52% (**Supplementary Fig. 40d**). Through SHAP analysis, we found that each biomarker category (pulse, GSR, metabolites, and electrolytes) provided non-overlapping and valuable information for stress and state anxiety level prediction.

Supplementary Note 9 | ML evaluations and metrics.

Metrics for binary and multiclass stress classification: confusion matrix, accuracy, precision-recall, and F_1 score.

Confusion matrix, also known as the error matrix, is a table that visualizes the accuracy between actual classes and predicted ones (**Supplementary Fig. 38c,d**). For binary classifications, the confusion matrix is represented by a positive and a negative class. True positive (TP) is defined when the prediction correctly indicates the positive class, and likewise true negative (TN) is defined for correctly predicted negative ones. False positive (FP) is defined when the prediction incorrectly indicates the positive class, and false negative (FN) is defined for incorrectly predicted negative class. For multiclass classifications, the confusion matrix is represented by the labeled classes.

Accuracy represents the total number of correct predictions over all predictions and is defined as:

$$Accuracy = \frac{TP + TN}{TP + TN + FP + FN}$$

However, accuracy may not be a good measure when the dataset is imbalanced, as a high accuracy in the majority class may lead the model to have a high overall accuracy even if other classes were predicted poorly. In our dataset, the relaxation state outweigh the stressed state, and using accuracy alone in our scenarios can result in misleading interpretation of high results.

Therefore, precision-recall is introduced along with their combination metric F_1 score, and is a better measure than accuracy. Precision is a measure of result relevancy, while recall is a measure of how many truly relevant results are returned, and they are defined as:

$$Precision = \frac{TP}{TP + FP}, \; Recall = \frac{TP}{TP + FN}$$

F_1 score is the harmonic mean of precision and recall:

$$F_1 \text{ score} = 2 \times \frac{Precision \times Recall}{Precision + Recall}$$

Precision-recall plot is displayed for model selection in binary stress/relaxation detection (**Supplementary Fig. 38b**), and F_1 score is displayed for the finalized model across different individuals (**Supplementary Fig. 38d**). For multiclass classifications, the precision-recall and F_1 score should represent across all classes. Two averaging techniques were taken: micro and macro-averaged precision-recall, where micro quantifies the scores on all classes jointly, and macro takes arithmetic mean of per-class. They are defined as:

$$Micro{:}Precision = \frac{\sum_{i=1}^{N} TP_{(\text{class } i)}}{\sum_{i=1}^{N} TP_{(\text{class } i)} + \sum_{i=1}^{N} FP_{(\text{class } i)}}, Recall = \frac{\sum_{i=1}^{N} TP_{(\text{class } i)}}{\sum_{i=1}^{N} TP_{(\text{class } i)} + \sum_{i=1}^{N} FN_{(\text{class } i)}}$$

$$Macro{:}Precision = \frac{1}{N}\sum_{i=1}^{N} Precision_{(\text{class } i)}, Recall = \frac{1}{N}\sum_{i=1}^{N} Recall_{(\text{class } i)}$$

where N denotes number of classes. The choices of metric depends on the ranking of the classes, since micro-averaging computes the proportion of correctly classified result over all observations (i.e., overall accuracy), and macro-average treats all classes in an equally weight. Both cases were used in our study. In model selection process, micro-averaged precision-recall is utilized for evaluating overall performance regardless of stress categories (**Fig. 4c**). In evaluating classification accuracy, on the other hand, macro-averaged F_1 score is displayed in **Fig. 4e** which evaluates performance in each stress type while micro-average is plagued to misleading interpretation of high results (**Supplementary Fig. 39a**).

Metrics for state anxiety level regression: mean squared error, R^2 score, and confidence level.

Mean squared error (MSE) measures the average of the squares of the errors between predicted and true values, which is one of the most widely used metrics for regression (**Supplementary Fig. 40b**).

R^2 score, also named as coefficient of determination, is another crucial statistical measure of regression. It measures the proportion of variation in the output dependent attribute that is predicted from the input independent variables, and tells how well the regression model fits the data. R^2 score is upper bounded by the value 1, attained for perfect fit (**Supplementary Fig. 40a**).

Confidence interval is defined as a range of estimates for an unknown parameter (herein, state anxiety level), and is calculated at a designated confidence level. Due to the natural standard deviation of questionnaire scores as aforementioned, we take ±2 anxiety points as the confidence interval buffer for state anxiety level evaluation. Confidence level is calculated accordingly after model training by the proportion of predicted values that falls within this range in testing dataset (**Fig. 4h**). We anticipate that for large-scale human trials with autonomic physiological signals collected from the CARES device can remove this bias, and provide a more robust stress assessment tool as a possible replacement of the questionnaires for stress quantification.

Feature importance evaluations using SHAP: After feature extraction, the feature importance of each biomarker was evaluated using Shapley additive explanation (SHAP) values, which utilizes a game theory approach to explain a feature's individual and overall contribution to the final prediction. Effectively, the SHAP value of a feature represents the average marginal contribution of the feature across the entire dataset (all prediction instances). To gain an understanding of how each biomarkers affect stress classification, we segmented the SHAP analysis across each stress

state (**Fig. 4g**, **Supplementary Fig. 39b,c**). Similarly, the SHAP contributions of each feature is shown in **Fig. 4i** and **Supplementary Fig. 40e** for state anxiety level prediction. Both figures indicate that while individual feature importance can vary across a dataset, there is no single feature that dominates the outcome. This SHAP analysis is extended in **Supplementary Fig. 39d**, **Fig. 4j** and **Supplementary Fig. 40f**, where the stress contribution of each feature starting from an initial average stress state is displayed. In our study, a low GSR profile plays a dominant role in the relaxation state in the ML model, followed by the sweat rate indicated by Na^+, heart rate indicated by pulse duration, and glucose concentration in sweat. For physiological stress induced with vigorous exercise, the pulse features such as heart rate, systolic and dicrotic peak waveforms have a major influence on stress classification, and lactate concentration in sweat also plays an important role. It can be inferred that due to natural sweat induction during extensive exercise, the GSR tracks mixed signals of not only sweat gland activity in skin but also sweat fluid conductivity itself, and therefore GSR may not be sufficient to distinguish exercise-induced stress for the ML model. For physiological stress in CPT that is induced without vigorous activities, the electrolyte concentrations including NH_4^+ and Na^+ as well as GSR have a dominant impact on model classification. As for the psychological VR challenge, while the heart rate increases similarly with that of vigorous exercise, GSR remains the key feature since no intense natural sweating occurred. As seen in the figures, there is no feature that dramatically alters or contributes an abnormally high contribution to the final stress prediction. Rather, each feature has a relative contribution to predict the final state anxiety score. This contribution may be large or small; however, no biomarker drastically outweighs the importance of another. This informs us that each feature is individually valuable to the final accuracy of the model, carrying relevant information that should not be discounted. Through the SHAP values, we gain a more in depth understanding of how each biomarker contributes to the stress across each experimental protocol.

Note that SHAP analysis is designed as a game theory approach in determining a biomarker's individual non-overlapping contribution to the prediction[117], and shows the relative significance in the model instead of building the absolute contribution to state anxiety. SHAP is in combination of all features that we understand what each feature is doing relatively to the model and tells us how much the model output changes when we change each input feature, instead of each feature's absolute role to final prediction objective. In our study, SHAP shows that these metabolites and electrolytes do hold non-overlapping information that contribute to the model.

Supplementary Table 1 | List of sweat metabolite sensors for on-body monitoring.

Analyte	Analytical method	Detection element	Layers	Stability	Stability in sweat	Reference
Glucose, lactate	Electrochemical-amperometry	GOx, LOx	Au/PB/chitosan-CNT-GOx, LOx	2 hours	2 hours	[67]
Glucose	Electrochemical-amperometry	GOx	Au/PB/NiHCF/agarose-chitosan-glycerol-GOx	20 hours	1.25 hours	[118]
Glucose	Electrochemical-amperometry	GOx	Graphene/PB/GOx/Nafion	6 hours	N/A	[119]
Glucose, lactate	Optical-colorimetry	GOx, LDH	GOx with iodide, LDH with diaphorase	6 hours	N/A	[120]
Glucose	Electrochemical-amperometry	GOx	GOx/carbon PB	1 hour	1 hour	[121]
Glucose	Electrochemical-amperometry	GOx	Au/ZnO/DSP/GOx antibody/GOx	4 hours	4 hours	[122]
Lactate	Electrochemical-amperometry	LOx	Carbon fiber/CNT-TTF/BSA-LOx/chitosan	8 hours	1 hour	[123]
Lactate	Electrochemical-amperometry	LOx	Graphite-PB/BSA-LOx/chitosan	2 hours	2 hours	[124]
UA	Electrochemical-differential pulse voltammetry	Oxidation current peak	Laser-engraved graphene	2 hours	2 hours	[125]
Glucose, lactate, UA	Electrochemical-amperometry	GOx, LOx, Uricase	Carbon/PB-NiHCF/BSA-GA-GOx, LOx, uricase	100 hours	100 hours	This work

GOx, glucose oxidase; LOx, lactate oxidase; PB, Prussian blue; CNT, carbon nanotube; TTF, tetrathiafulvalene; LDH, lactate dehydrogenase; GA, glutaraldehyde.

Supplementary Table 2 | List of sweat electrolyte sensors for on-body monitoring.

Analyte	Substrate	Functional materials	ISM matrix	Stability	Stability in sweat	Reference
Na^+	Screen-printed carbon	Carbon	PVC/DOS	2.8 mV h^{-1}	1 hour	[126]
Na^+, K^+	Au	PEDOT:PSS	PVC/DOS	2–3 mV h^{-1}	2 hours	[67]
K^+	Glassy carbon	PEDOT:PSS	Silicone rubber/PVC/DOS	0.14 mV min^{-1}	N/A	[68]
K^+	Screen-printed carbon	Ferrocyanide/PEDOT:PSS	PVC/DOS	0.8 mV h^{-1}	N/A	[127]
K^+	Carbon/Graphite	Single-walled CNT	Poly(n-butylacrylate)	0.19 mV h^{-1}	N/A	[128]
Na^+	Au	Au nanodendrites	PVC/DOS	0.22 mV h^{-1}	2 hours	[129]
K^+, Ca^{2+}, H^+	Graphene paper	Graphene paper	PVC/o-NPOE	1.92–2.27 mV h^{-1}	N/A	[130]
NH_4^+	Screen-printed Ag	Screen-printed carbon	PVC/o-NPOE	N/A	1 hour	[57]
Na^+, K^+	PB analogues (Na-NiHCF, K-FeHCF)	PB analogues (Na-NiHCF, K-FeHCF)	PVC/o-NPOE or PVC/DOS	10–50 mV day^{-1}	N/A	[131]
Na^+, K^+, NH_4^+	Inkjet carbon	Carbon nanoparticles	SEBS/PVC/DOS	0.04 mV h^{-1}	100 hours	This work

PVC, polyvinyl chloride; DOS, bis(2-ethylhexyl) sebacate; LEG, laser-engraved graphene; o-NPOE, o-nitrophenyl octyl ether.

Supplementary Table 3 | List of pulse features extracted for ML pipelines.

Feature name	Feature description
systolicPeakTime	The time duration from the start of the pulse to the systolic peak.
tidalPeakTime	The time duration from the start of the pulse to the tidal peak.
dicroticPeakTime	The time duration from the start of the pulse to the dicrotic peak.
pulseDuration	The time duration from the start to the end of the pulse, which is inverse to heart rate.
pAIx	The peripheral augmentation index (pAIx) is a measurement of arterial stiffness, considering the amplitude ratio of the first reflected wave over the systolic waveform. pAIx has been correlated with cardiovascular disease and cholesterol. Height, gender, and age may all effect pAIx. pAIx may also be referred to as the radial augmentation index in the literature. $$pAIx = \frac{tidalPeakAmp}{systolicPeakAmp}$$
reflectionIndex	The reflection index (RIx) is influenced by the vascular tone and the endothelium's (arterial lining's) condition. Higher RI values indicate a stressed endothelium. RI values can be influenced by caffeine and exercise. RI may also be referred to as the diastolic augmentation index in the literature. $$RIx = \frac{dicroticPeakAmp}{systolicPeakAmp}$$

Supplementary Table 4 | List of ML accuracy for stress and state anxiety monitoring using wearables.

Sensors	Model	Subjects	Y/N Classify Accuracy	Stressor Classify Accuracy	Stress/State Anxiety Level Accuracy	References
2 separate physical (ECG, GSR, EMG, Resp, T, Acc)	linear discriminant analysis	15	92.28%	79.57%	N/A	[109]
Physical (PPG, GSR, T, Acc)	SVM	5	95%	N/A	N/A	[111]
Physical (ECG, SC, Resp)	Bayesian network	13	84%	N/A	N/A	[132]
ECG	CNN+RNN	13, 9	87.39%, 73.96%	N/A	N/A	[133]
Physical (HR, GSR)	CNN	10	91.8%	N/A	N/A	[134]
GSR	SVM	9	73.41%	N/A	N/A	[135]
Physical (HRV, Resp)	logistic regression	10	81%	N/A	N/A	[136]
Physical (GSR, Acc)	logistic regression	12	91.66%	N/A	N/A	[137]
Physical (HRV, GSR, T)	random forest	32	94.52%	78.15%	81.82%, 82.70% for low and high stress	[83]
Physical (ECG, EMG, GSR, Resp)	linear discriminant analysis	32	94.7%, 97.4%	N/A	N/A	[138]
Physical (Pulse, GSR, T) + Chemical (glucose, lactate, UA, Na^+, K^+, NH_4^+)	random forest XGBoost	10	99.2%	98.0%	98.7%	This work

ECG, electrocardiogram. GSR, galvanic skin response. EMG, electromyography. Resp, respiration. T, temperature. Acc, Acceleration. PPG, photoplethysmogram. BVP, blood volume pulse.
CNN, convolutional neural network. LSTM, long short-term memory. SVM, support vector machine. RNN, recurrent neural network.

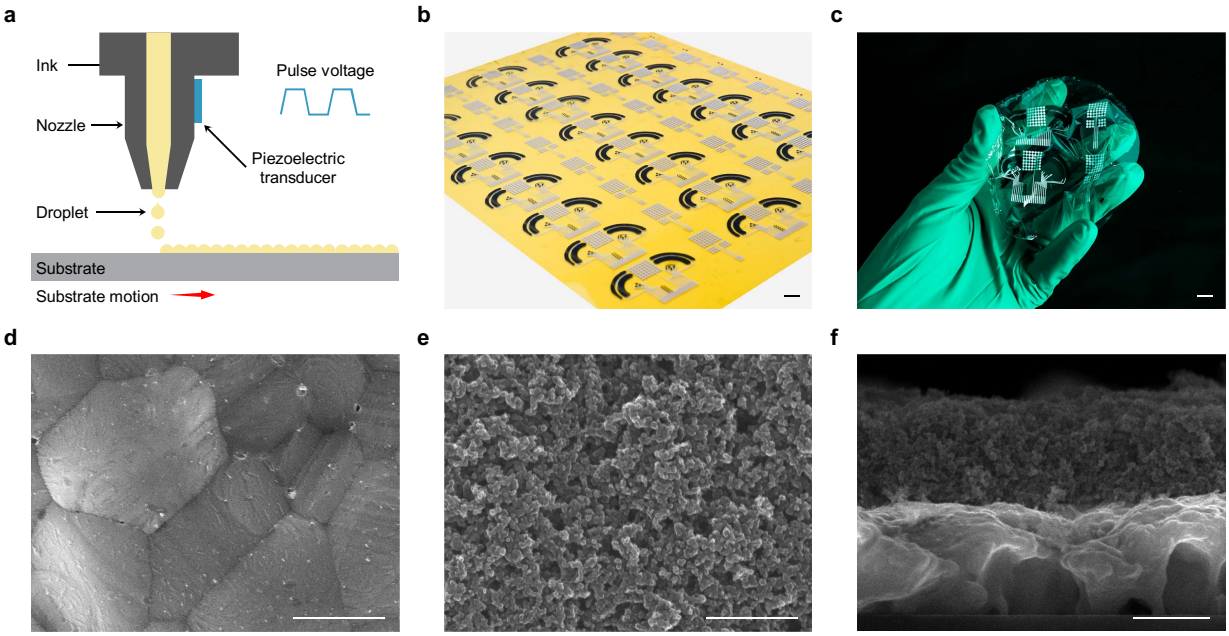

Supplementary Fig. 1 | Characterization of the inkjet-printed CARES electrodes. a, Schematics of inkjet printing mechanism. **b**, Optical image of a flexible CARES sensor array fabricated via mass-producible and low-cost inkjet printing. Scale bar, 1 cm. **c**, Optical image of an ultrathin CARES patch on a subject hand. Scale bar, 1 cm. **d**–**f**, SEM images of inkjet-printed Ag (**d**), carbon (**e**), and cross-section of Ag-carbon interconnect (**f**). Scale bars, 500 nm.

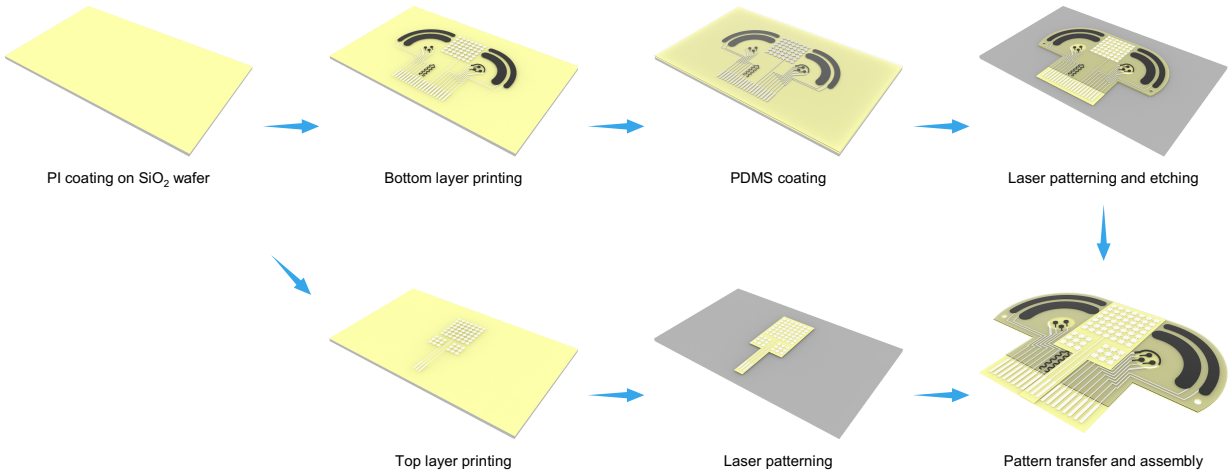

Supplementary Fig. 2 | Fabrication process of the flexible CARES patch.

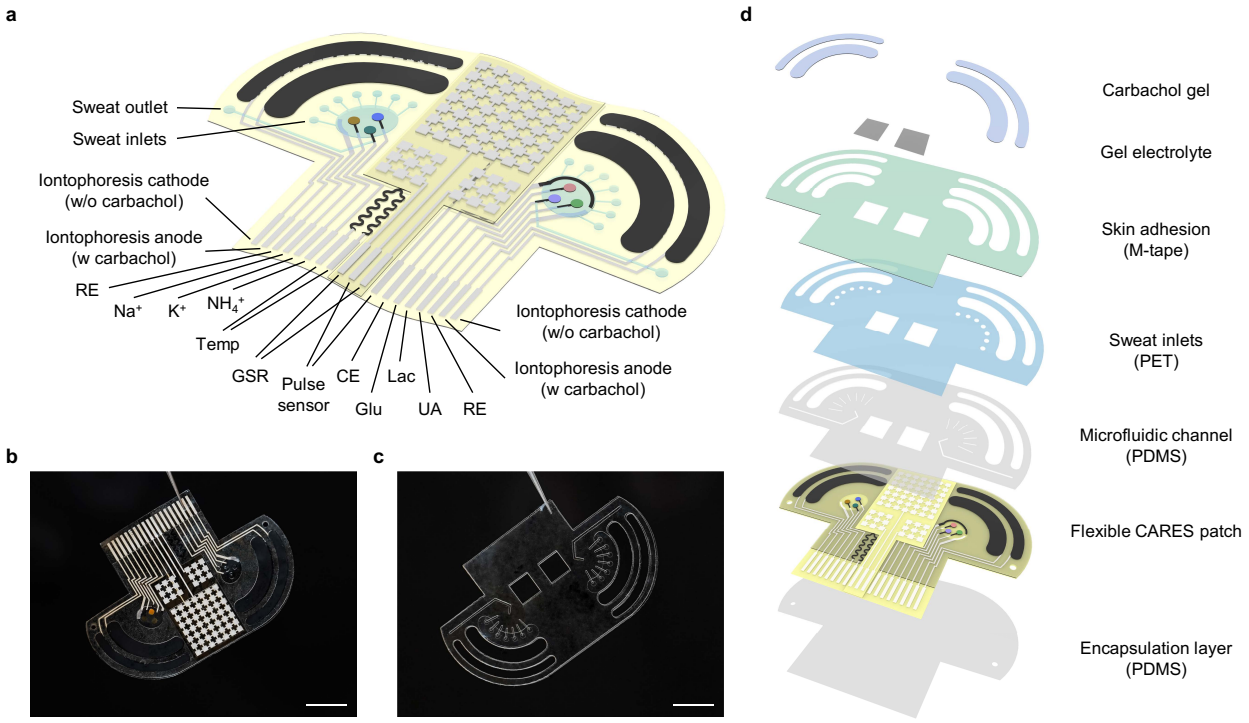

Supplementary Fig. 3 | Layered assembly of microfluidic CARES system. a, Detailed sensor configurations and pin assignments of the CARES. **b**,**c**, Optical images of CARES sensor patch after biochemical sensors preparation (**b**) and the microfluidics module (**c**). Scale bars, 1 cm. **d**, The layer breakdown of the CARES system.

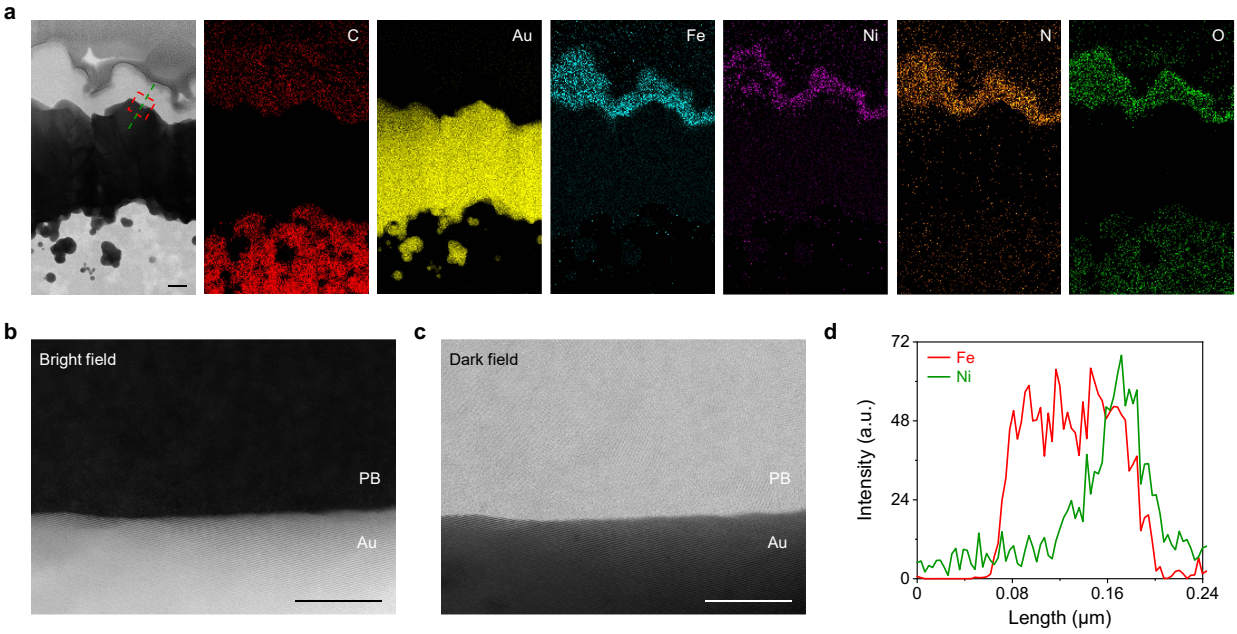

Supplementary Fig. 4 | Characterizations of PB-NiHCF nanostructures. a, STEM and corresponding EDS mapping images for inkjet-printed carbon/AuNPs/PB-NiHCF cross-sectional layers. Scale bar, 100 nm. **b**,**c**, Bright field (**b**) and dark field (**c**) STEM images of Au/PB-NiHCF interfaces. Scale bar, 10 nm. **d**, Statistical distribution of Fe and Ni atoms based on the EDS.

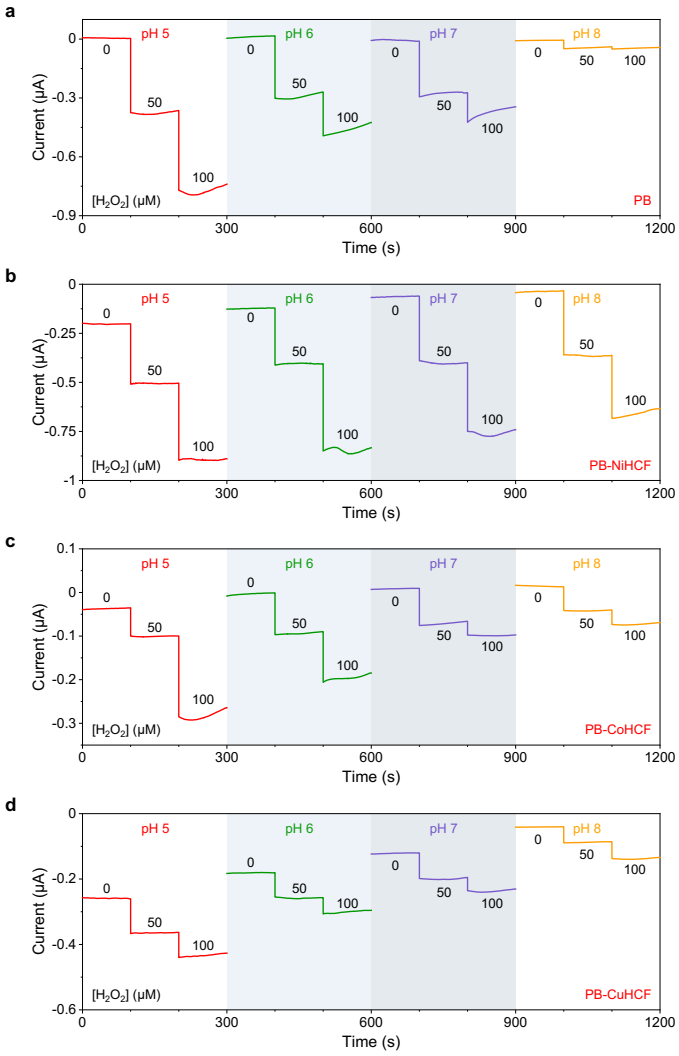

Supplementary Fig. 5 | Electrochemical characterizations of PB, PB-NiHCF, PB-CoHCF, and PB-CuHCF against degradation. a–d, Chronoamperometric responses of PB (**a**), PB-NiHCF (**b**), PB-CoHCF (**c**), and PB-CuHCF (**d**) electrodes in the presence of McIlvaine buffer solutions containing 0, 50, and 100 μM H_2O_2.

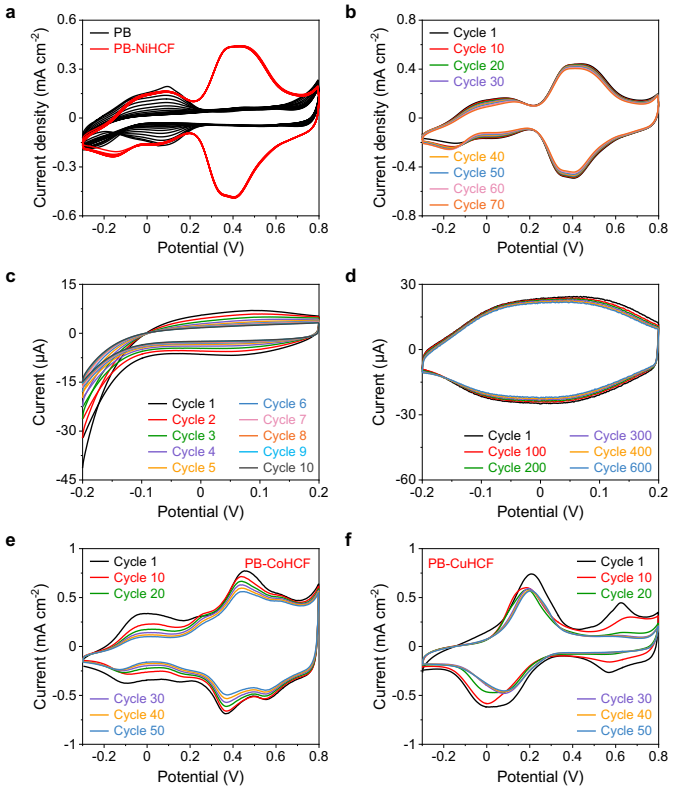

Supplementary Fig. 6 | Electrochemical characterizations of PB, PB-NiHCF, PB-CoHCF, and PB-CuHCF against ion insertion. a, Cyclic voltammetry (CV) scans of PB and PB-NiHCF electrodes from -0.2 V to 0.8 V for 15 cycles. Scan rate, 50 mV s^{-1}. **b**, CV scans of PB-NiHCF electrodes from -0.2 V to 0.8 V for 70 cycles. Scan rate, 50 mV s^{-1}. **c**, CV scans of PB electrodes from -0.2 V to 0.2 V for 10 cycles. Scan rate, 50 mV s^{-1}. **d**, CV scans of PB-NiHCF electrodes from -0.2 V to 0.2 V for 600 cycles. Scan rate, 50 mV s^{-1}. **e,f**, CV scans of PB-CoHCF and PB-CuHCF electrodes from -0.3 V to 0.8 V for 50 cycles.

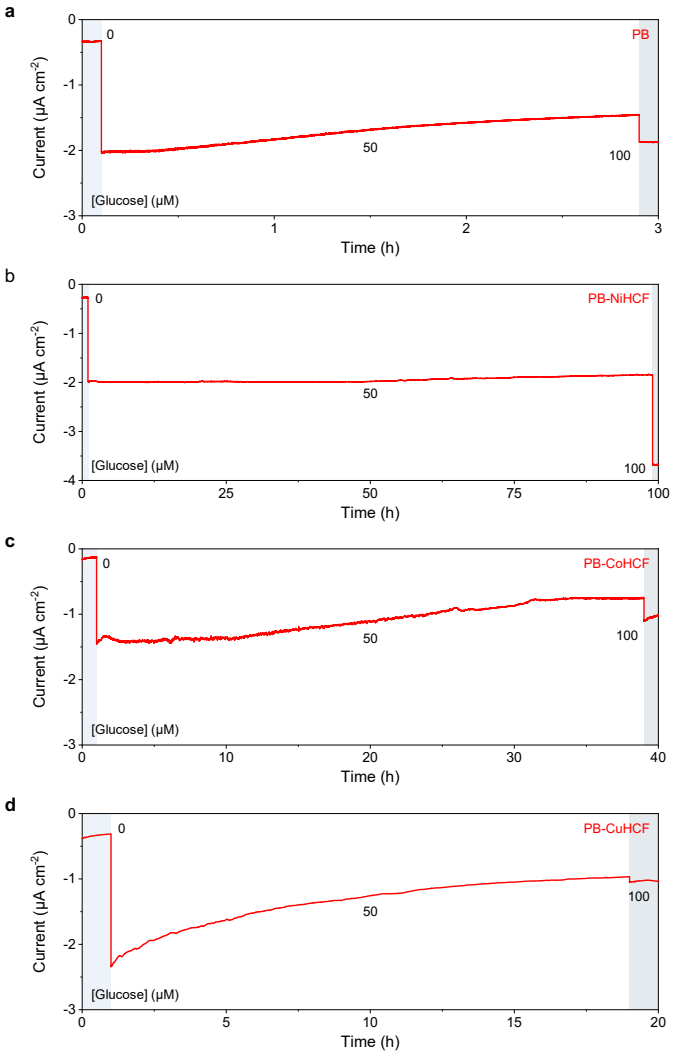

Supplementary Fig. 7 | The long-term stability test for PB, PB-NiHCF, PB-CoHCF, and PB-CuHCF based glucose sensors. a–d, Amperometric responses of glucose sensors based on PB (**a**), PB-NiHCF (**b**), PB-CoHCF (**c**), and PB-CuHCF (**d**) in PBS solutions containing 0, 50, 100 μM glucose.

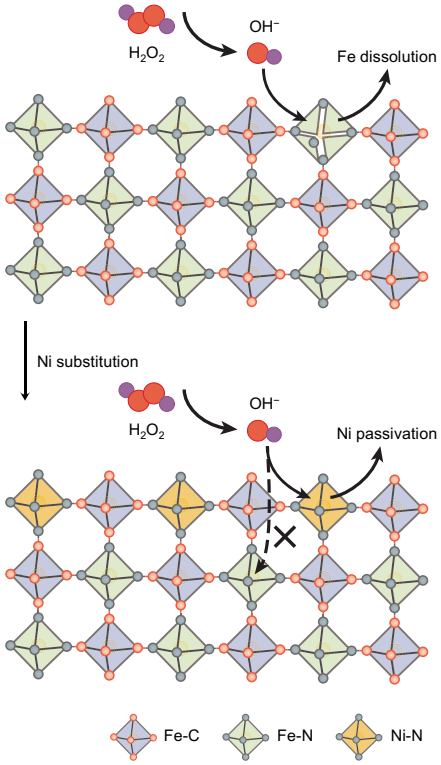

Supplementary Fig. 8 | Schematic of passivation mechanism of PB-NiHCF. Hydroxide ions (OH^-) can break Fe−(CN)−Fe bond while nickel serves as protection layer to prevent PB degradation.

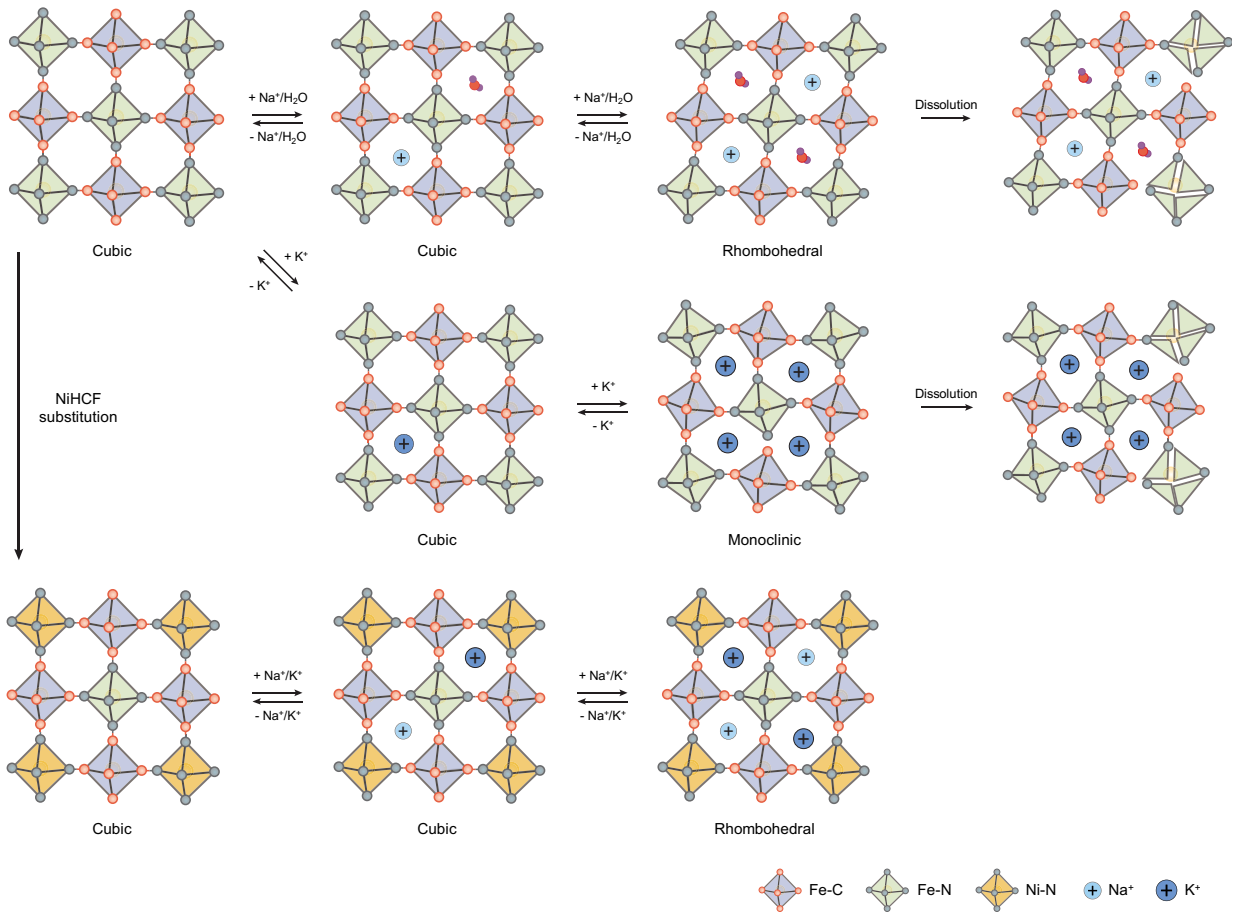

Supplementary Fig. 9 | Schematic of ion intercalation mechanism of PB and PB-NiHCF. Cubic PB structure can distort from to a less symmetric rhombohedral or monoclinic geometry, while nickel substitution could reduce lattice constant and suppress structure distortion.

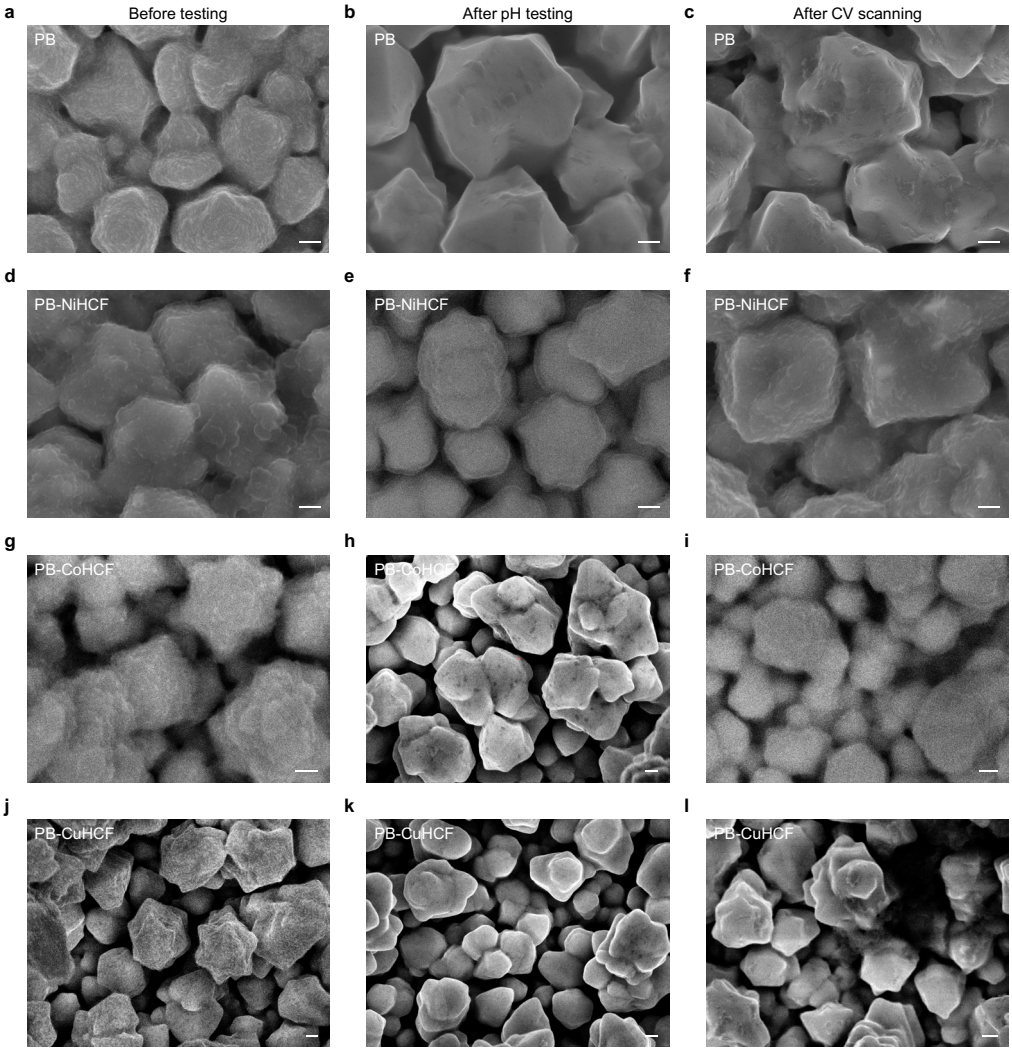

Supplementary Fig. 10 | Microscopic characterizations of the long-term stability of PB-NiHCF, PB-CoHCF, and PB-CuHCF. a–c, SEM images of PB deposited on grown AuNPs on inkjet carbon electrodes before testing (**a**), after testing in alkaline McIlvaine buffer solutions (**b**), and after 15 cycles of CV scans between -0.2 V and 0.5 V in PBS (**c**). Scale bars, 100 nm. **d–f**, SEM images of PB-NiHCF deposited on grown AuNPs on inkjet carbon electrodes before testing (**d**), after testing in alkaline McIlvaine buffer solutions (**e**), and after 1000 cycles of CV scans between -0.2 V and 0.5 V in PBS (**f**). Scale bars, 100 nm. **g–i**, SEM images of PB-CoHCF deposited on grown AuNPs on inkjet-printed carbon electrodes before testing (**g**), after testing in alkaline McIlvaine buffer solutions (**h**), and after 15 cycles of CV scans between -0.2 V and 0.5 V in PBS (**i**). Scale bars, 100 nm. **j–l**, SEM images of PB-CuHCF deposited on grown AuNPs on inkjet-printed carbon electrodes before testing (**j**), after testing in alkaline McIlvaine buffer solutions (**k**), and after 15 cycles of CV scans between -0.2 V and 0.5 V in PBS (**l**). Scale bars, 100 nm.

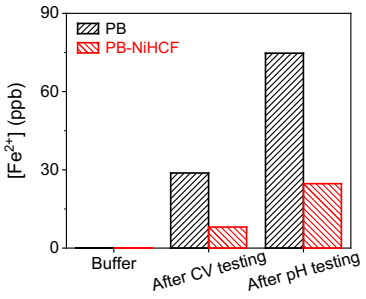

Supplementary Fig. 11 | Inductively coupled plasma–mass spectrometry (ICP–MS) analysis of Fe^{2+} after testing of the PB and PB-NiHCF electrodes. The electrodes were tested in the alkaline McIlvaine buffer solutions or in PBS solutions with CV scans from -0.2 V to 0.2 V for 10 cycles.

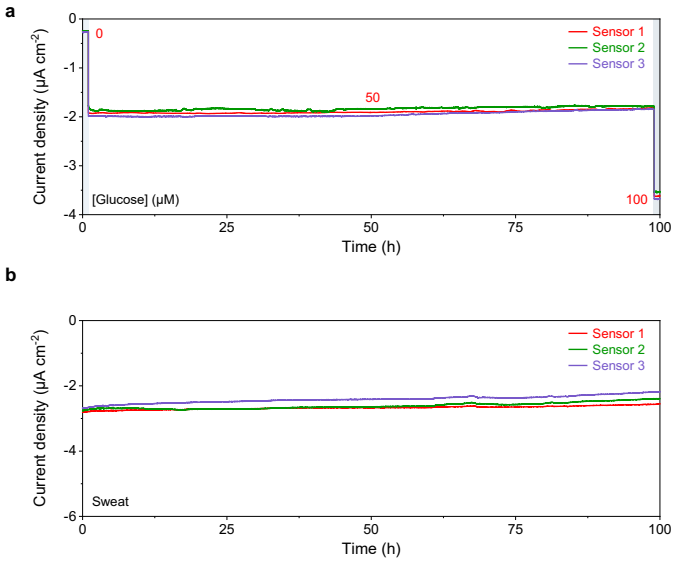

Supplementary Fig. 12 | Long-term stability of continuous 100-hour in vitro tests of wearable glucose biosensors. a,**b**, Amperometric response of the glucose sensors tested in standard solution (**a**) and untreated human sweat samples (**b**) over 100 hours.

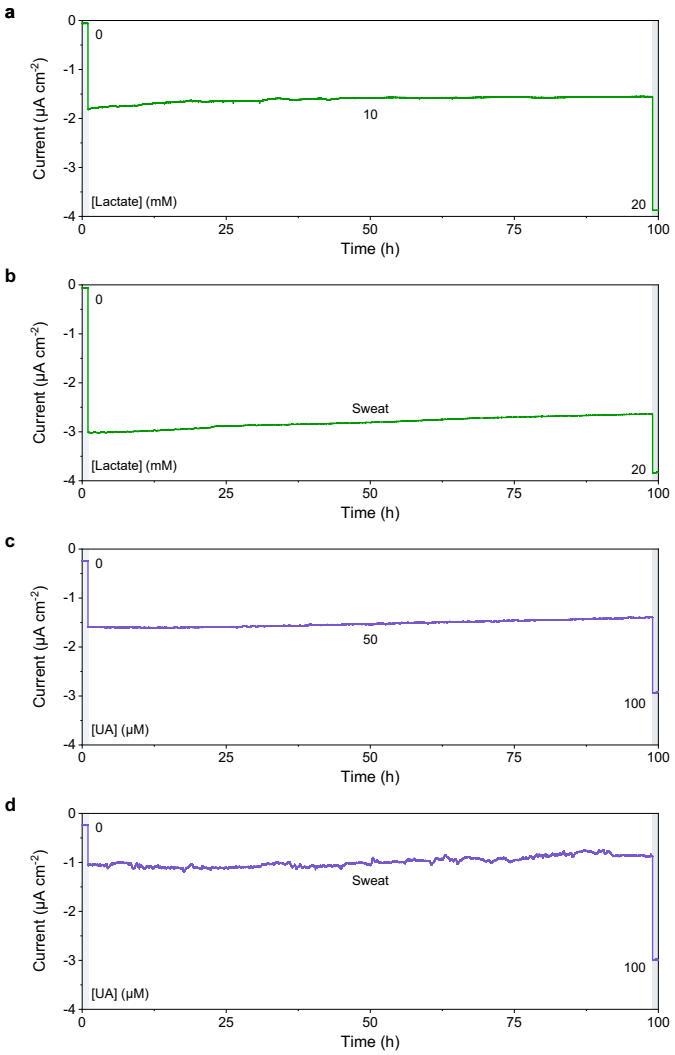

Supplementary Fig. 13 | Long-term stability of continuous 100-hour in vitro tests of wearable lactate and UA biosensors. a,**b**, Amperometric response of the lactate sensors tested in PBS solutions (**a**) and untreated human sweat samples (**b**) over 100 hours. **c**,**d**, Amperometric response of the UA sensors tested in PBS solutions (**c**) and untreated human sweat samples (**d**) over 100 hours.

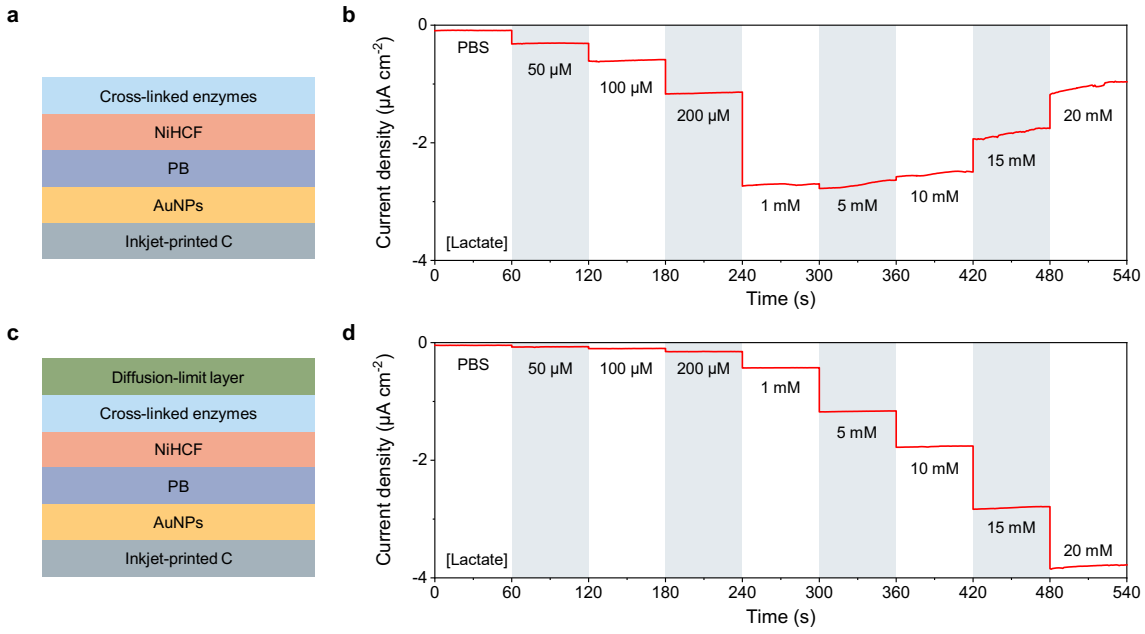

Supplementary Fig. 14 | Evaluation of the diffusion-limit layer for lactate sensing. a,**b**, Schematic of lactate sensors based on Au/PB-NiHCF (**a**) and the corresponding amperometric performance in lactate solutions (0–20 mM) (**b**). **c**,**d**, Schematic of introduction of diffusion-limit PVC/DOS membrane over enzyme film (**c**) and the corresponding amperometric performance in lactate solutions (0–20 mM) (**d**).

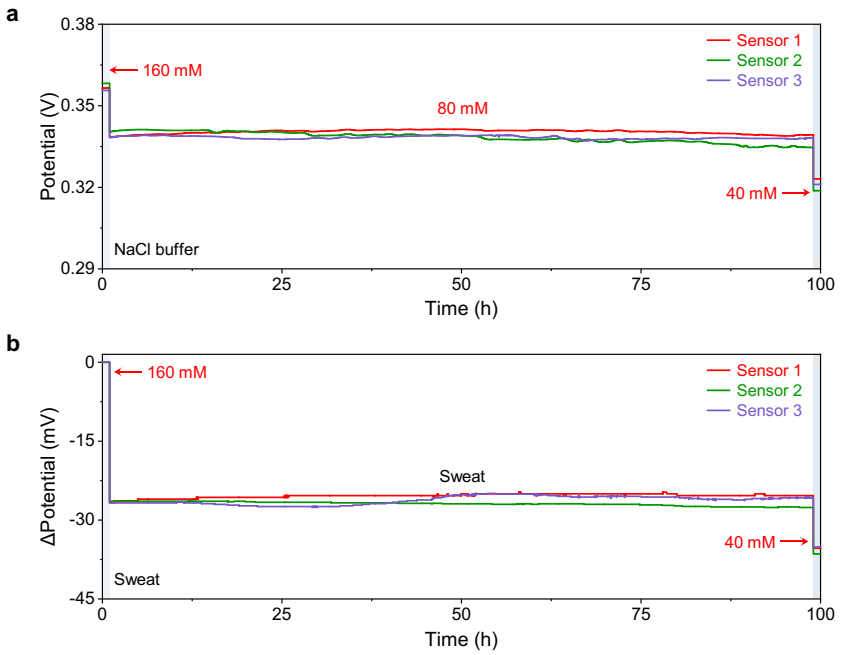

Supplementary Fig. 15 | Long-term stability of continuous 100-hour in vitro tests of wearable ISE-based Na^+ sensor. a,**b**, Potentiometric responses of Na^+ sensors tested in standard solution (**a**) and untreated human sweat samples (**b**) over 100 hours.

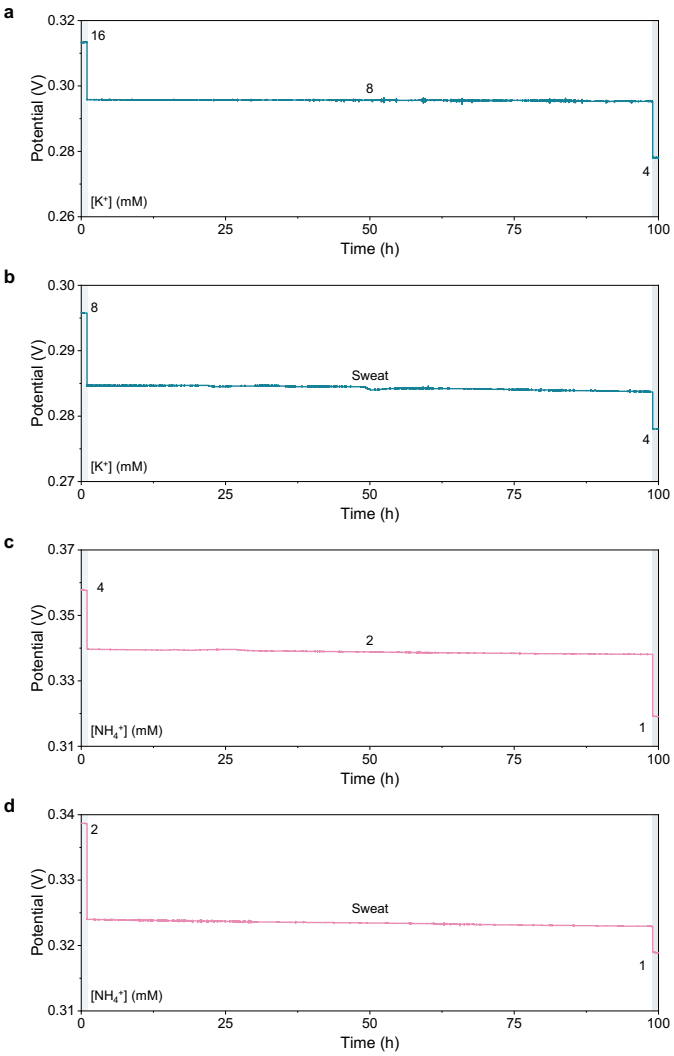

Supplementary Fig. 16 | Long-term stability of continuous 100-hour in vitro tests of wearable ISE-based K^+ and NH_4^+ sensor. a,**b**, Potentiometric responses of K^+ sensors tested in standard solutions (**a**) and untreated human sweat samples (**b**) over 100 hours. **c**,**d**, Potentiometric responses of NH_4^+ sensors tested in standard solutions (**c**) and untreated human sweat samples (**d**) over 100 hours.

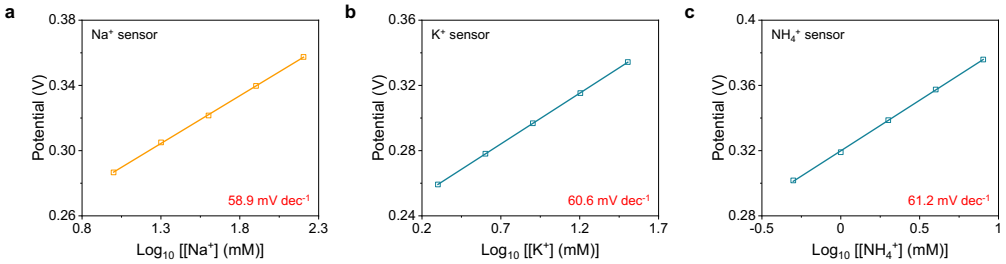

Supplementary Fig. 17 | The calibration plots of the ion-selective sensors. The plots are generated based on the sensor data demonstrated in Fig. 2f.

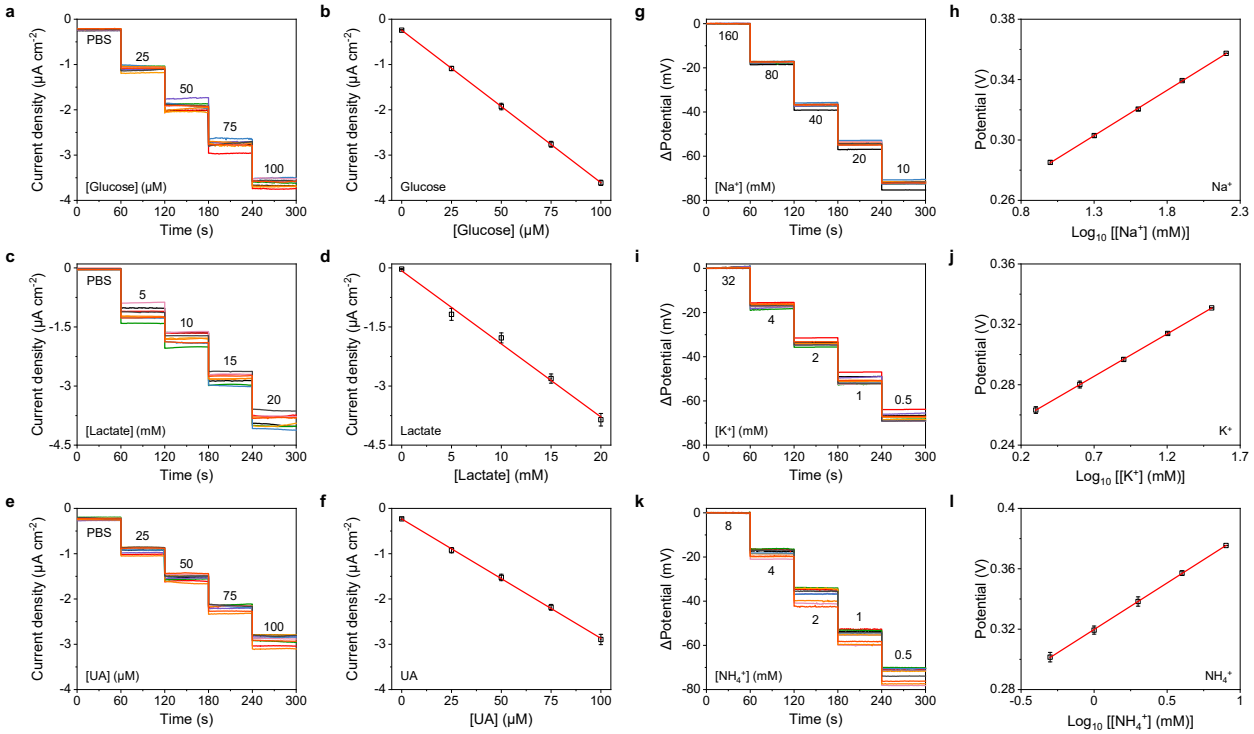

Supplementary Fig. 18 | Reproducibility of biochemical sensors in the CARES. a–l, Batch to batch variation of glucose (**a,b**), lactate (**c,d**), UA (**e,f**), Na^+ (**g,h**), K^+ (**i,j**), and NH_4^+ (**k,l**) sensors. Data is presented as mean ± SD (n = 10 sensors for each category).

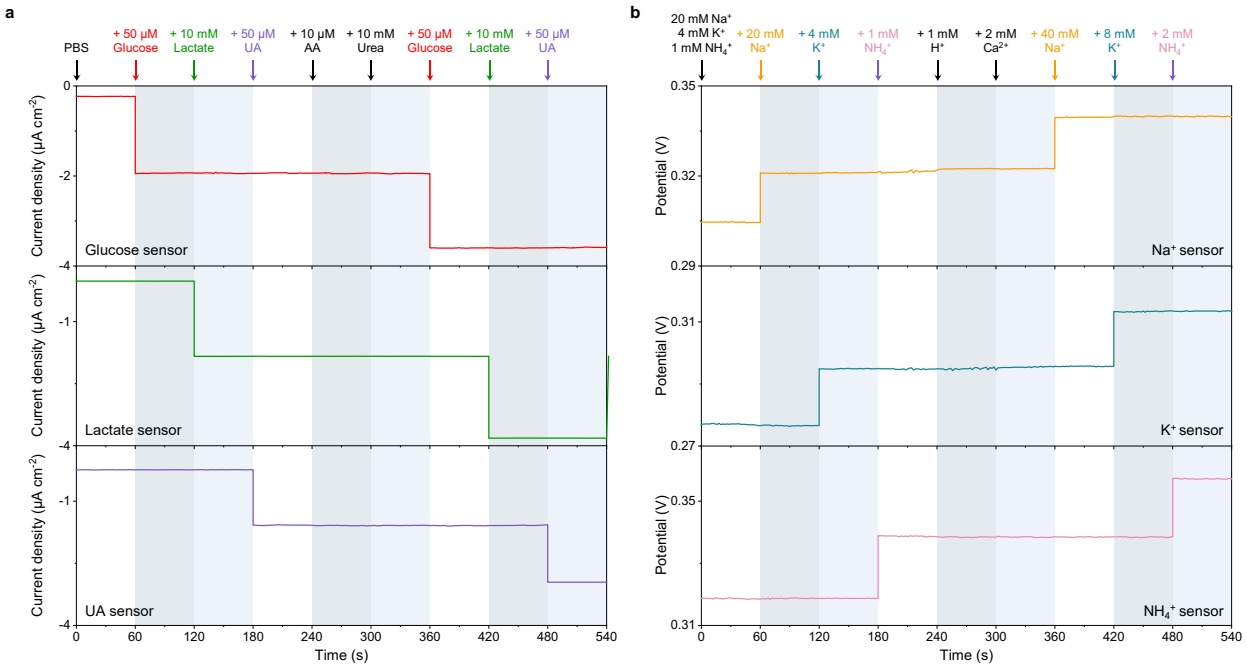

Supplementary Fig. 19 | Selectivity of enzymatic and ISE sensors. a,**b**, Interference study for enzymatic glucose, lactate and UA sensors (**a**), and ion-selective Na^+, K^+, NH_4^+ sensors (**b**). Physiologically relevant levels of common sweat components were added to standard solution. AA, ascorbic acid.

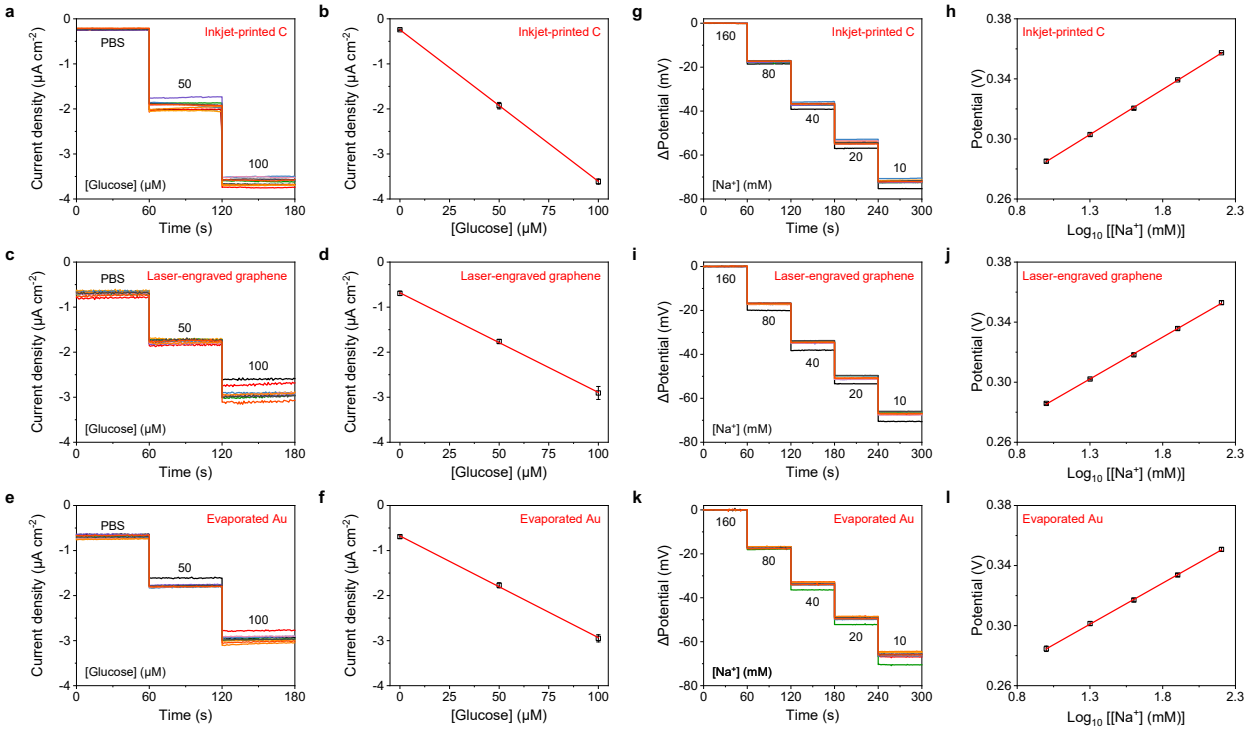

Supplementary Fig. 20 | The performance of biosensors based mass-producible inkjet-printed carbon, laser-engraved graphene, and evaporated Au electrodes. a−f, Amperometric responses of the glucose sensors based on inkjet-printed carbon (**a,b**), laser-engraved graphene (**c,d**), and evaporated Au electrodes (**e,f**) in PBS solutions containing 0−100 μM glucose. **g−l**, Potentiometric responses of the Na^+ sensors based on inkjet-printed carbon (**g,h**), laser-engraved graphene (**i,j**),and evaporated Au electrodes (**k,l**) in 10−160 mM Na^+ solutions. The sensing films were prepared using the same approach as **Fig. 2c,f**. Data is presented as mean ± SD (n = 10 sensors for each category).

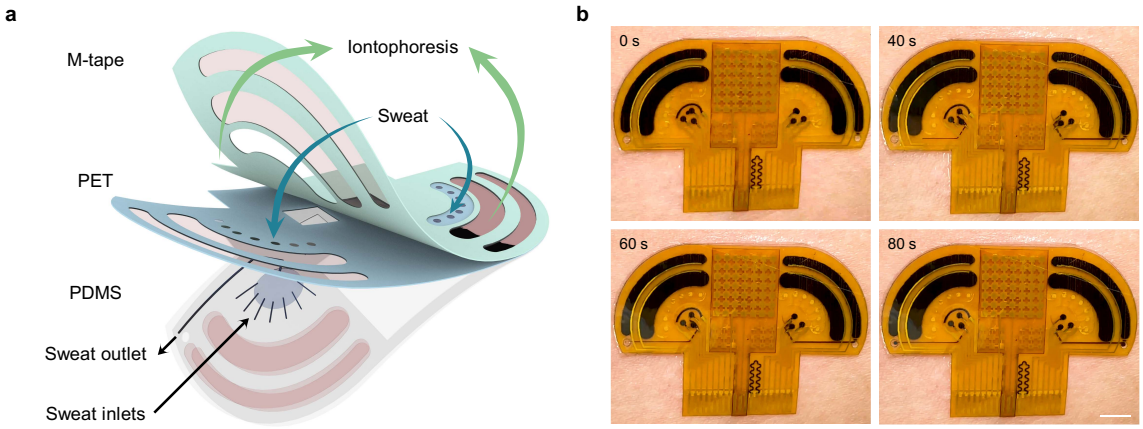

Supplementary Fig. 21 | Evaluation of the iontophoresis microfluidic module for autonomous sweat induction and sampling. a, Schematic of microfluidics module. **b**, Optical images of the two-reservoir microfluidic module during an iontophoresis-induced sweat secretion process. Scale bar, 5 mm.

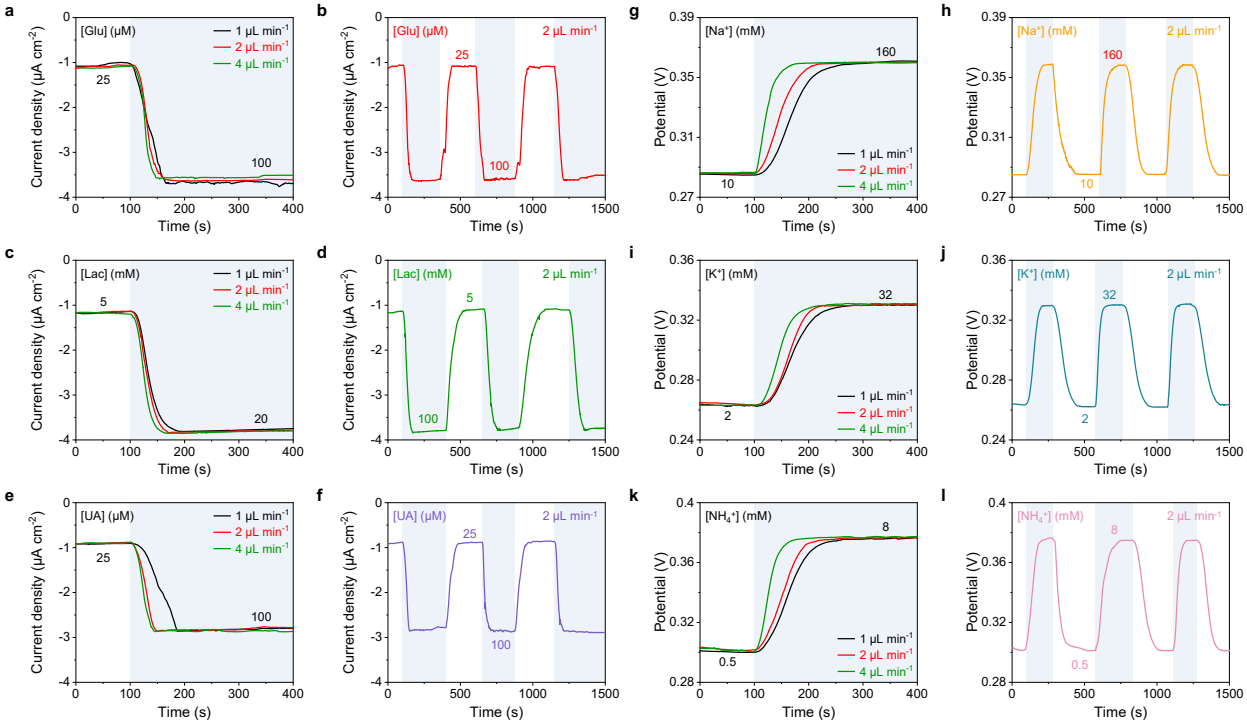

Supplementary Fig. 22 | Characterization of continuous microfluidic sensing performance under dynamic sweat flow. a–l, Dynamic response with a varying flow rate of 1−4 μL min^{-1} and repeatability of glucose (**a,b**), lactate (**c,d**), UA (**e,f**), Na^+ (**g,h**), K^+ (**i,j**), and NH_4^+ (**k,l**) sensors upon switching the inflow solutions.

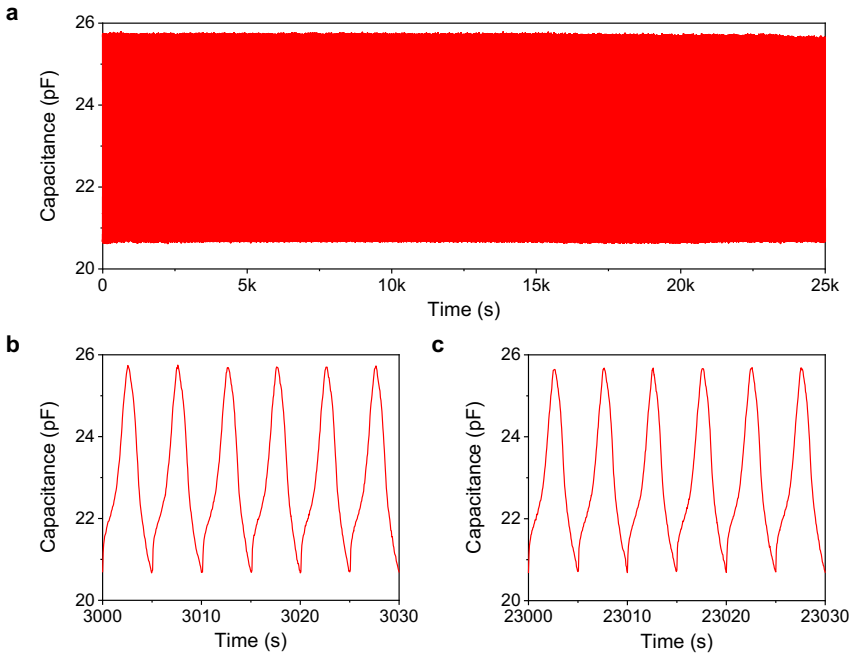

Supplementary Fig. 23 | Long-term stability of capacitive pressure sensor. a, A repetitive pressure-loading test involving 5,000 pressing-releasing cycles was performed. **b**,**c**, Dynamic pressure sensor response during 600−606 cycles (**b**) and 4,600−4,606 cycles (**c**) of pressing-releasing.

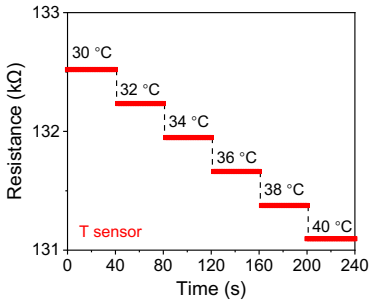

Supplementary Fig. 24 | Response of the temperature (T) sensor in the physiological temperature range.

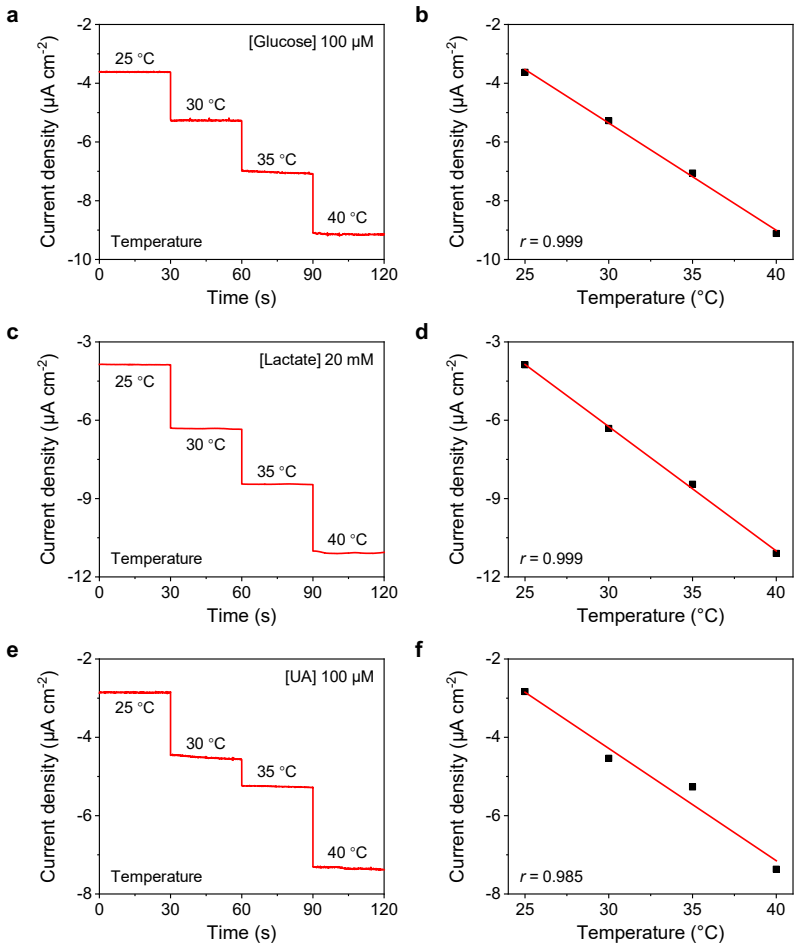

Supplementary Fig. 25 | Temperature influence on enzymatic sensors. a–**f**, Calibration of glucose (**a**,**b**), lactate (**c**,**d**), and UA (**e**,**f**) biosensors under physiologically relevant range of temperature.

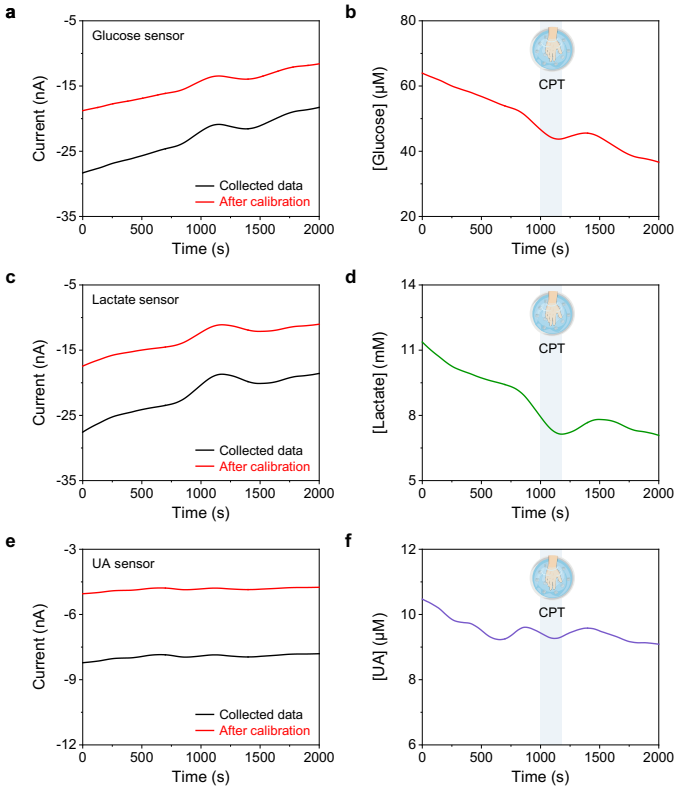

Supplementary Fig. 26 | Temperature calibration of the wearable enzymatic biosensors during the on-body experiments.

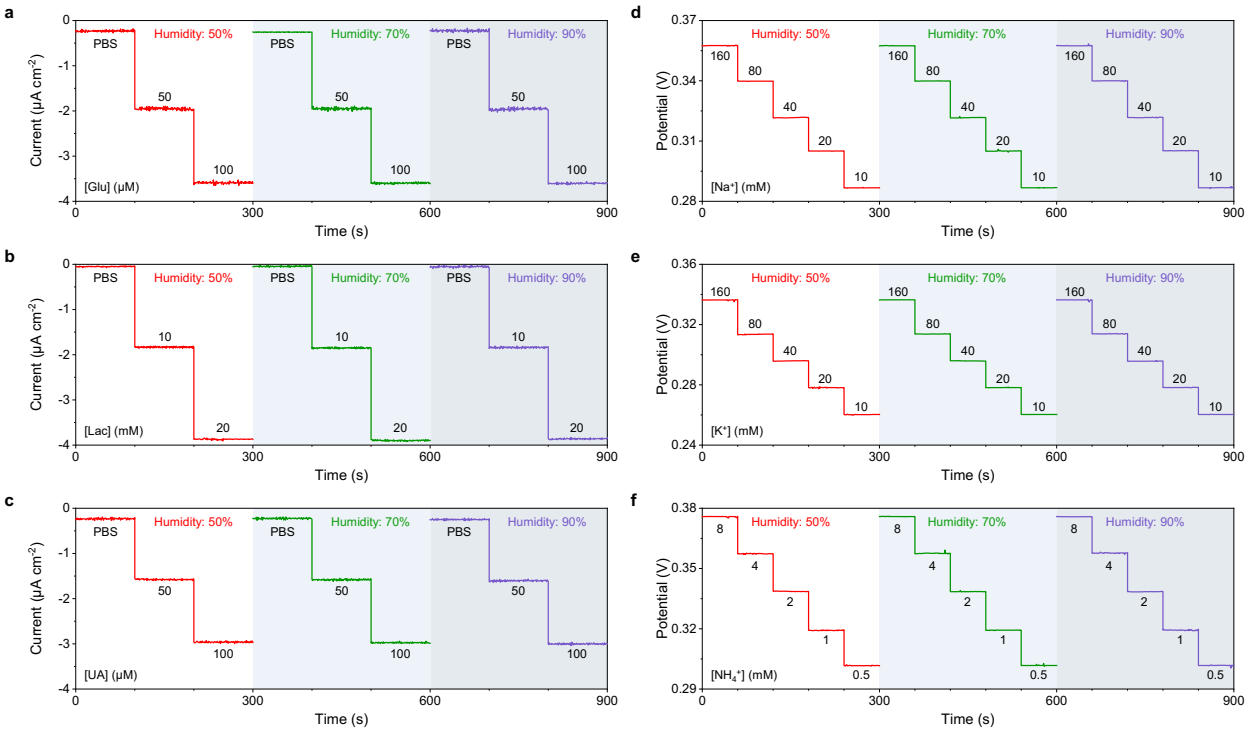

Supplementary Fig. 27 | Performance of PB-NiHCF electrodes and ISEs against environmental factors (i.e., humidity). The tests were performed in a plastic chamber with humidity controlled via water mist spray.

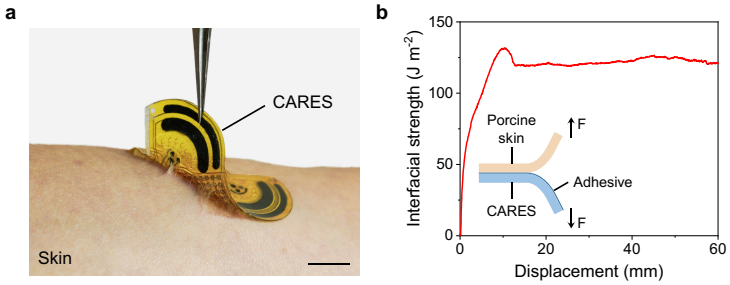

Supplementary Fig. 28 | Characterization of the adhesion of the CARES device to the skin. **a**, Optical image of a CARES device adhered onto the skin. **b**, Interfacial strength between porcine skin and the device adhered by medical adhesive.

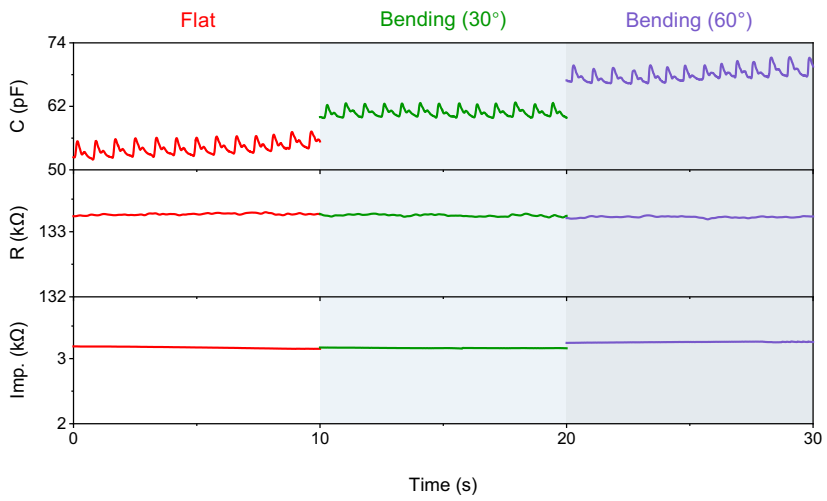

Supplementary Fig. 29 | Performance of all physical sensors of the CARES under mechanical bending strain test. Pulse, GSR and temperature sensors were attached to a healthy subject's wrist while a wide range of 0−60° wrist bending angles were applied.

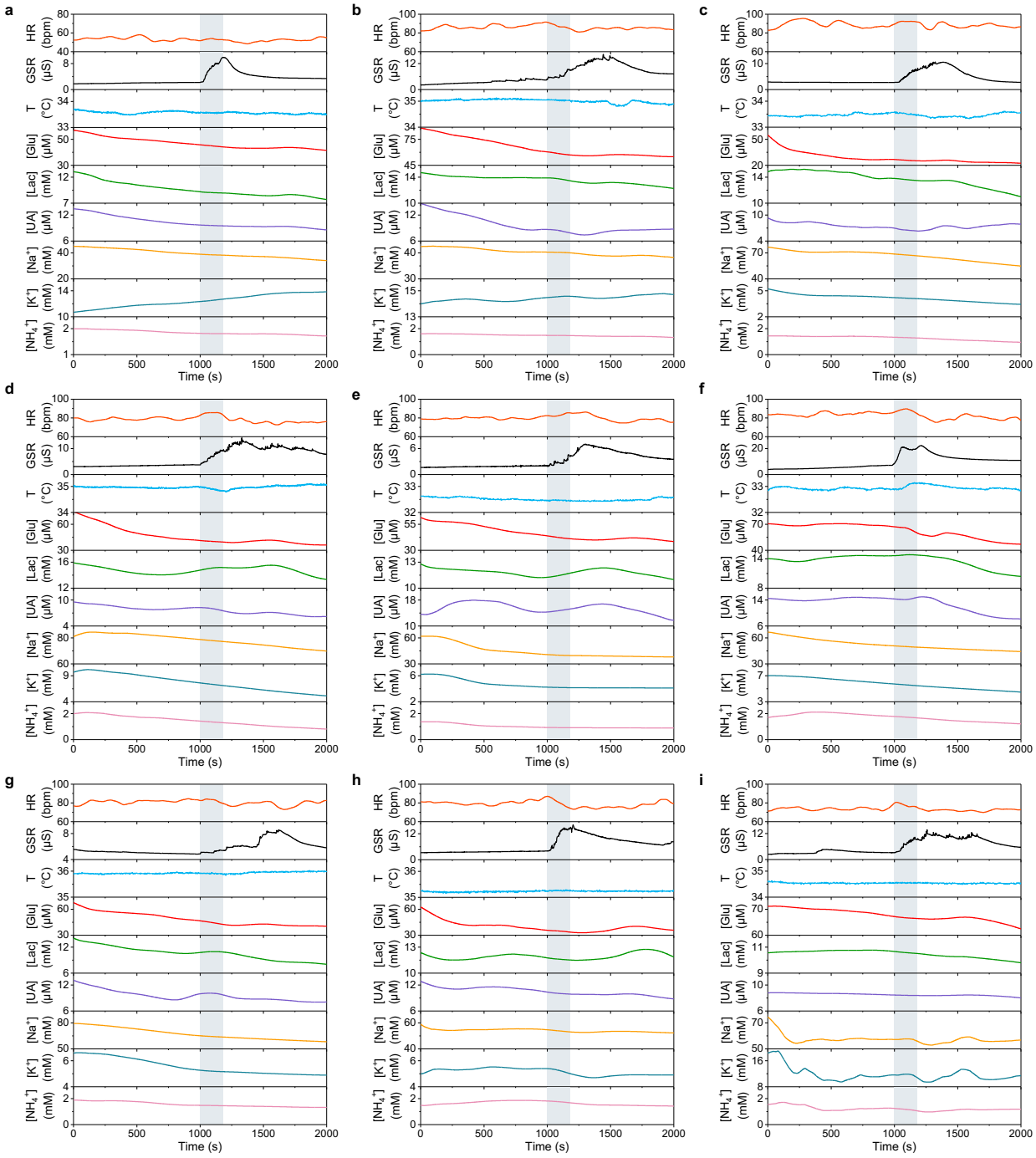

Supplementary Fig. 30 | On-body multimodal monitoring of CPT stress response. a–i, Multimodal sensor responses of CPT stress response in nine healthy subjects using the CARES.

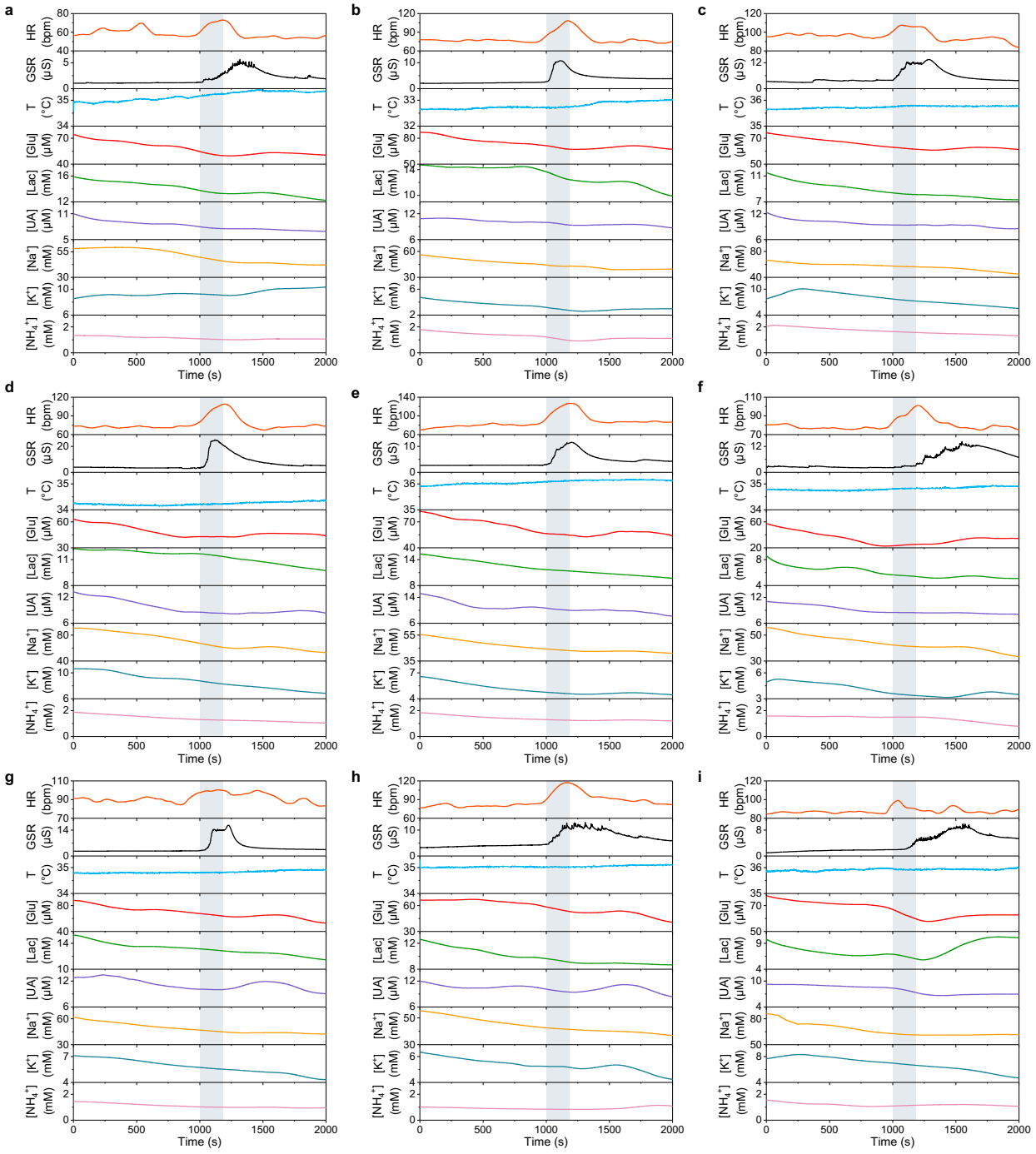

Supplementary Fig. 31 | On-body multimodal monitoring of VR challenge stress response. **a–i,** Multimodal sensor responses of VR challenge stress response in nine healthy subjects using the CARES.

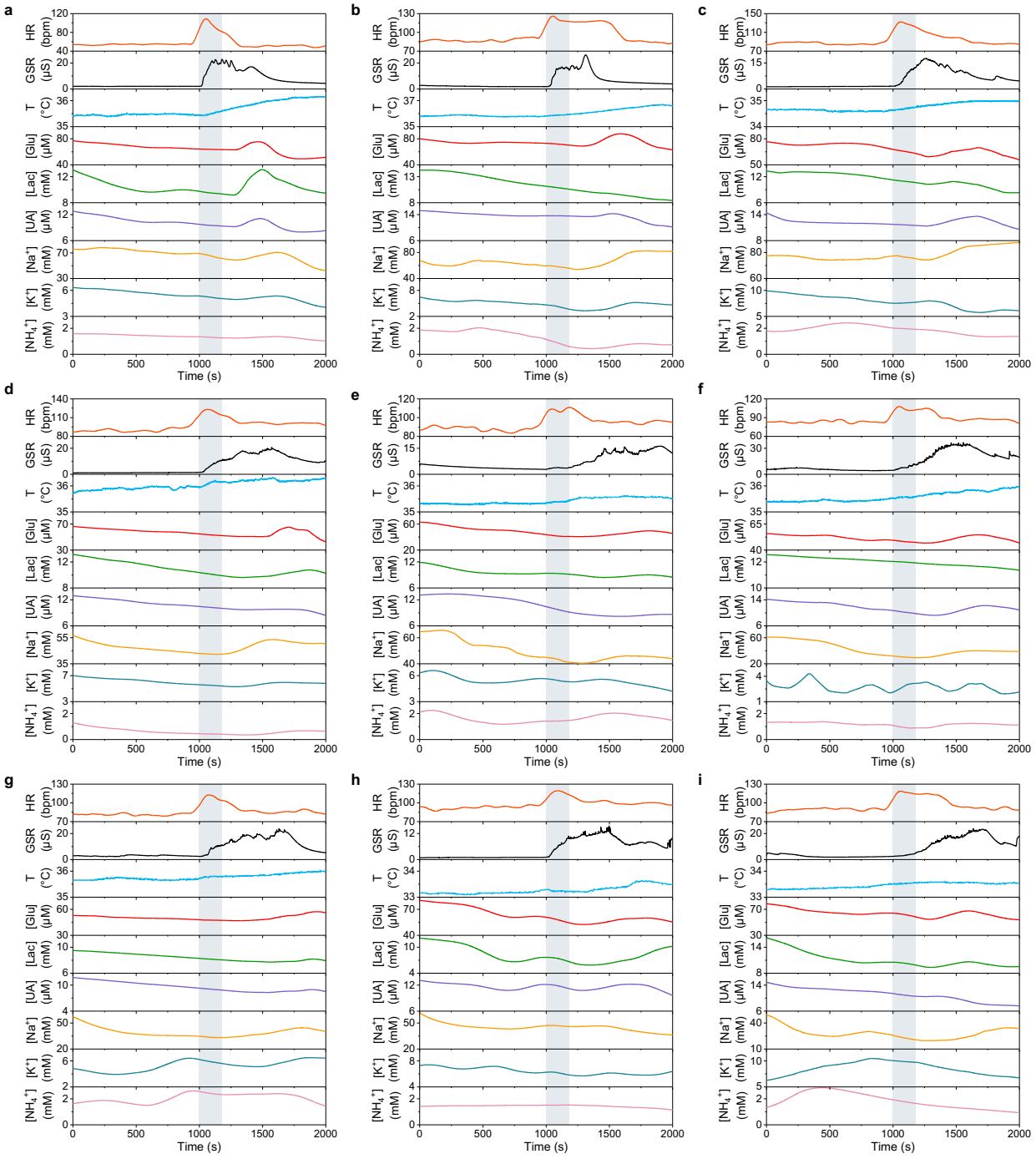

Supplementary Fig. 32 | On-body multimodal monitoring of exercise stress response. a–i, Multimodal sensor responses of exercise stress response in nine healthy subjects using the CARES.

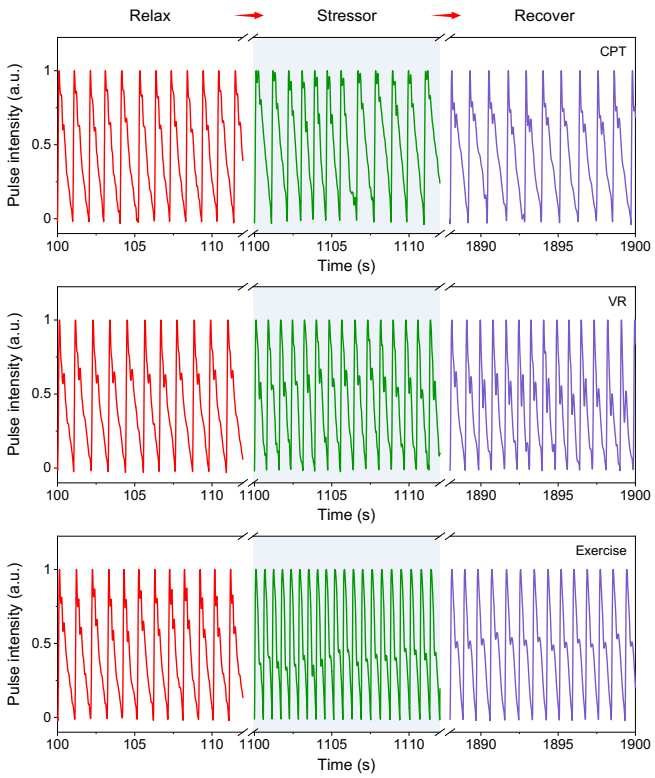

Supplementary Fig. 33 | Pulse waveform stress response monitoring of three stressors of a healthy subject. An autonomous pulse normalization algorithm was adopted, where each pulse waveform is normalized according to their systolic peak intensity amplitude.

a

Subject ID	Gender	Age	Height (cm)	Weight (kg)	BMI (kg m^{-2})
1	M	38	177	67	21.4
2	M	32	173	75	25.1
3	M	26	173	61	20.4
4	F	32	171	60	20.5
5	F	23	160	45	17.6
6	M	24	180	65	20.1
7	M	26	178	75	23.7
8	M	26	164	55	20.4
9	M	28	178	71	22.4
10	M	31	185	95	27.8

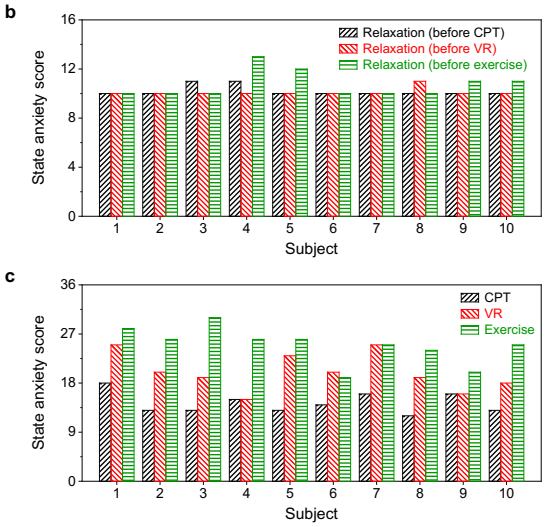

Supplementary Fig. 34 | Subject information involved in the stress human studies and corresponding state anxiety scores using STAI-Y questionnaires. a, Subjects health profiles including their age, gender, height, weight and body mass index (BMI). **b**, Raw questionnaire score from subjects indicating state anxiety levels during relaxation state. **c**, Raw questionnaire score from subjects indicating state anxiety levels during stressors.

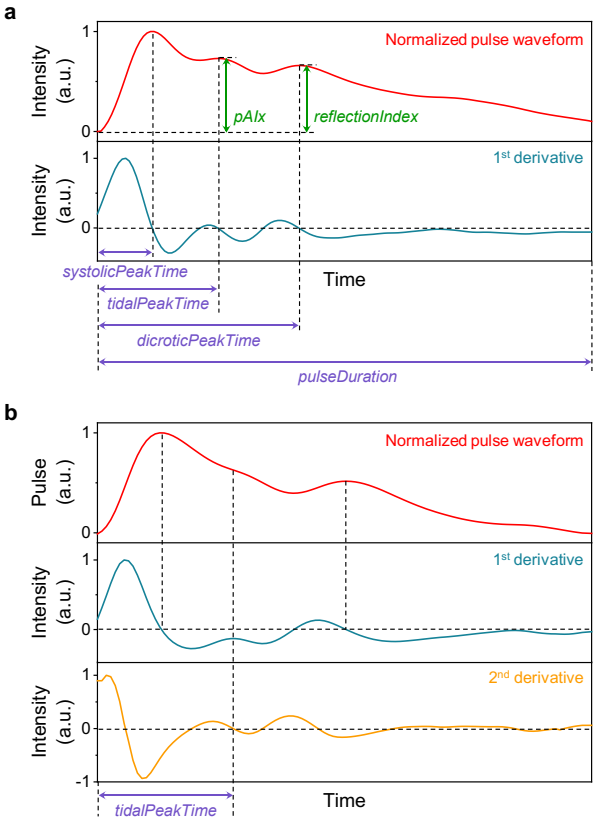

Supplementary Fig. 35 | Feature extraction from pulse waveform. a, A peak finding algorithm locating systolic, tidal and dicrotic peaks based on their 1st derivative. The algorithm first separates and normalizes each pulse waveform, then performs 1st derivative analysis and locate the unique peaks. **b**, An exception consideration to find tidal peaks based on the 2nd derivative. In practice, some subjects demonstrated vague tidal peaks, in which the 1st derivative cannot find tidal peak, and a 2nd derivative analysis was adopted to locate the inflection point.

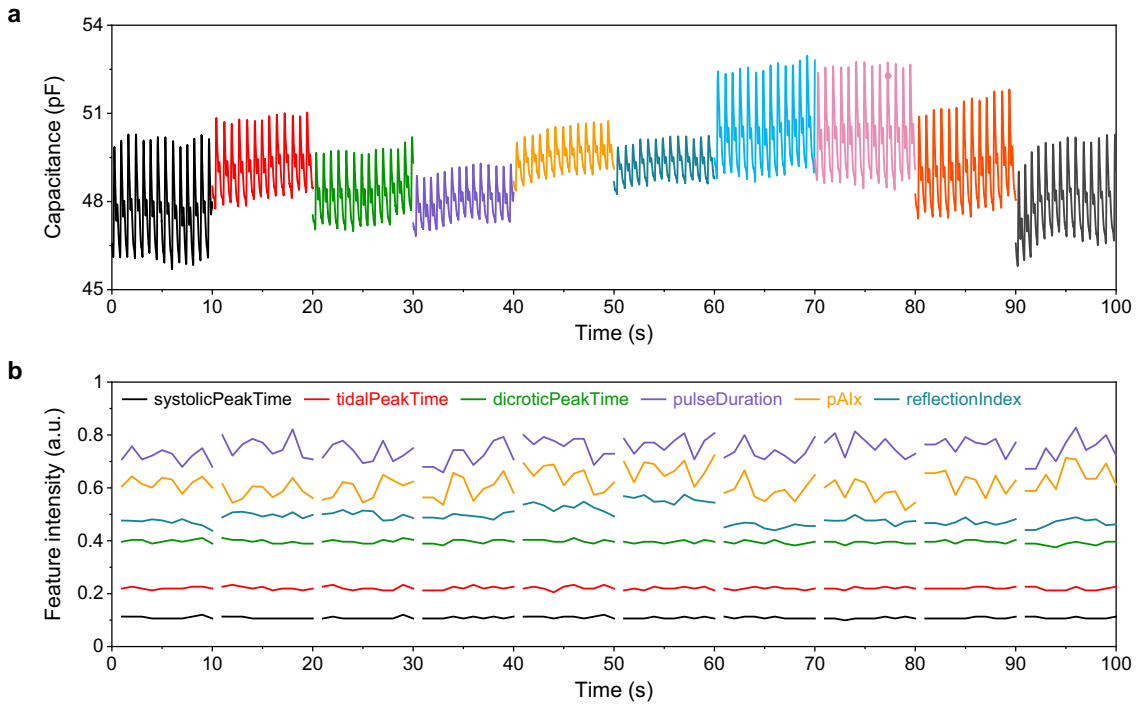

Supplementary Fig. 36 | Different patch placed on the same location of a relaxed subject's wrist and corresponding extracted features. a, Pulse signal variations due to fabrication and placement variations, which is inevitable. **b**, After feature extraction algorithm, the feature remained stable with negligible variations against patch variations.

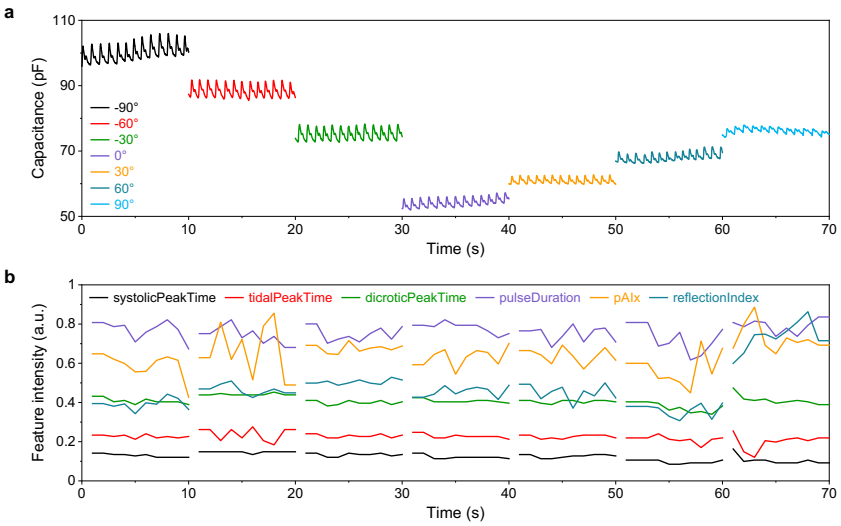

Supplementary Fig. 37 | Pulse signals measured at different wrist angles of a relaxed subject and corresponding extracted features. a, Pulse signal variations when the subject bends the wrist from -90° to 90°, which showed big waveform changes and could cause big variations during daily activities. **b**, After feature extraction algorithm, the feature remained stable in a moderate angle range from -30° to 30°.

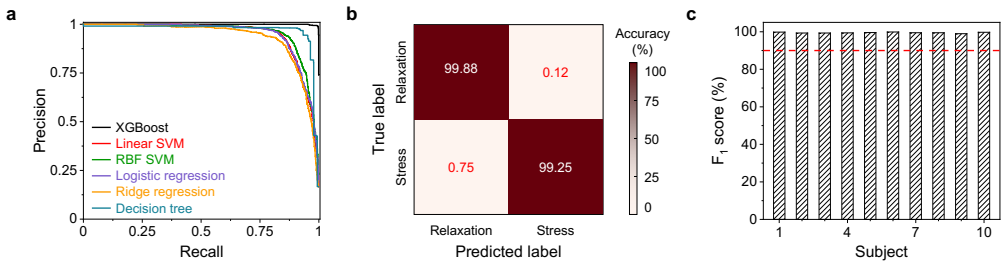

Supplementary Fig. 38 | ML prediction performance of stress detection. a, Precision-recall curve of different ML models for stress detection. XGBoost model outperforms other models in terms of precision-recall. SVM, support vector machine. RBF, radial basis function. **b**, Confusion matrix of a XGBoost model to the unseen test dataset. XGBoost achieved 99.25% accuracy of detecting stress and relaxation state, showing that it can generalize to classify unseen samples. **c**, The overall testing accuracy based on F_1 score for each involved subject.

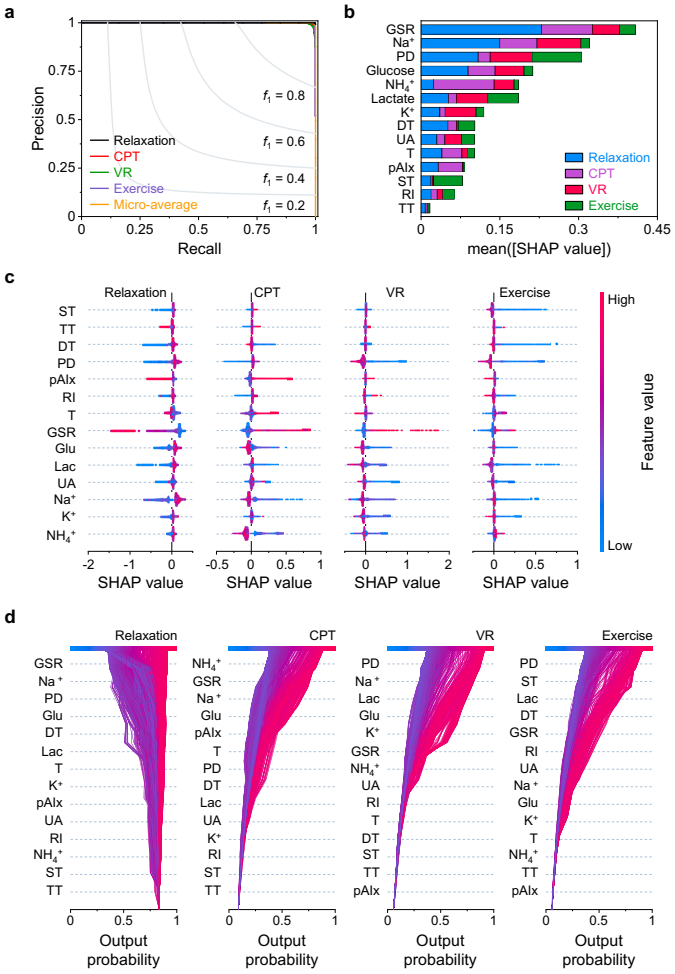

Supplementary Fig. 39 | ML prediction performance of stressor type classification. a, Precision-recall curve of a XGBoost model for each stressor as well as micro-averaged classification result. **b**, Stacked bar plot of feature importance showing their contribution to each stressor type. **c**, Shapley additive explanation (SHAP) summary plot with respect to a XGBoost model based on the dataset collected by CARES. **d**, SHAP decision plot explaining how a XGBoost model arrives at each stressor classification for every data point using both physiological and chemical features. Each decision line tracks the features contributions to every individual classification.

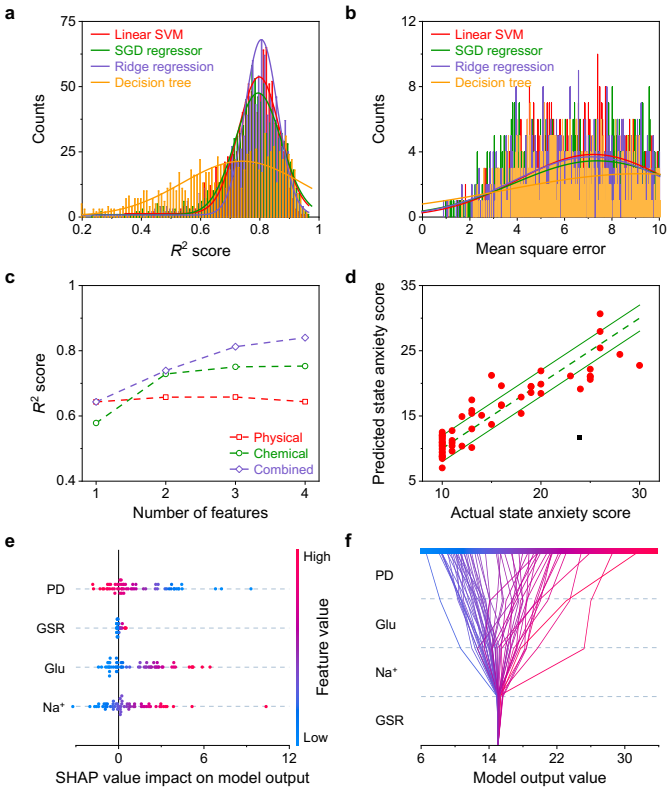

Supplementary Fig. 40 | ML performance of simple linear models for overall state anxiety level evaluation. a, R^2 score distribution for representative linear models over 1,000 runs of randomly splitting training and testing datasets to reduce uncertainties in reduced size of dataset. SGD, stochastic gradient descent. **b**, Mean-squared error (MSE) distribution for representative linear models over 1,000 runs. **c**, Brute-force feature selection and evaluation in a linear regression model with ridge regularization. The combination of physicochemical features outperformed that of physical and chemical sensors alone. **d**, True versus ML-predicted state anxiety score based on the linear model. ±2 state anxiety score buffer is shown based on the potential error in the state anxiety questionnaires. **e**, SHAP summary plot of the linear regression model based on the dataset collected by CARES. **f**, SHAP decision plot explaining how the linear model determines the state anxiety level using both physiological and biochemical features.

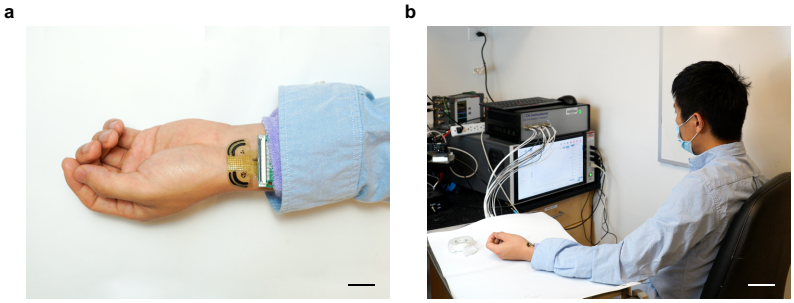

Supplementary Fig. 41 | Optical image of a healthy subject wearing a CARES patch for continuous data collection during the laboratory human studies. The CARES was connected to laboratory instruments via flexible cables. Scale bars, 2 cm and 10 cm for **a** and **b**, respectively.

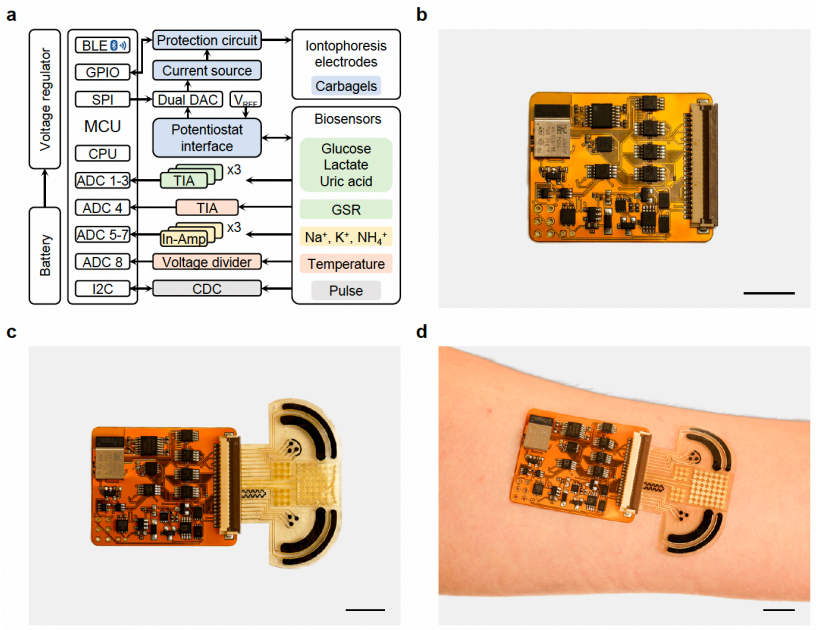

Supplementary Fig. 42 | Fully integrated wearable wireless CARES system for continuous data collection. a, System-level block diagram of the wireless wearable CARES system. BLE, Bluetooth Low Energy; GPIO, general purpose input/output; SPI, Serial Peripheral Interface; CPU, central processing unit; MCU, microcontroller; ADC, analogue-to-digital converter; TIA, trans-impedance amplifier; DAC, digital-to-analogue converter; CDC, capacitance-to-digital converter; I2C, Inter-Integrated Circuit; In-Amp, instrumentation amplifier. **b**,**c**, Photographs of a flexible printed circuit board (FPCB) for multimodal signal processing (**b**) and an assembled wireless wearable CARES system (**c**). **d**, Photograph of a wireless wearable CARES system worn on the ventral forearm. Scale bars, 1 cm.

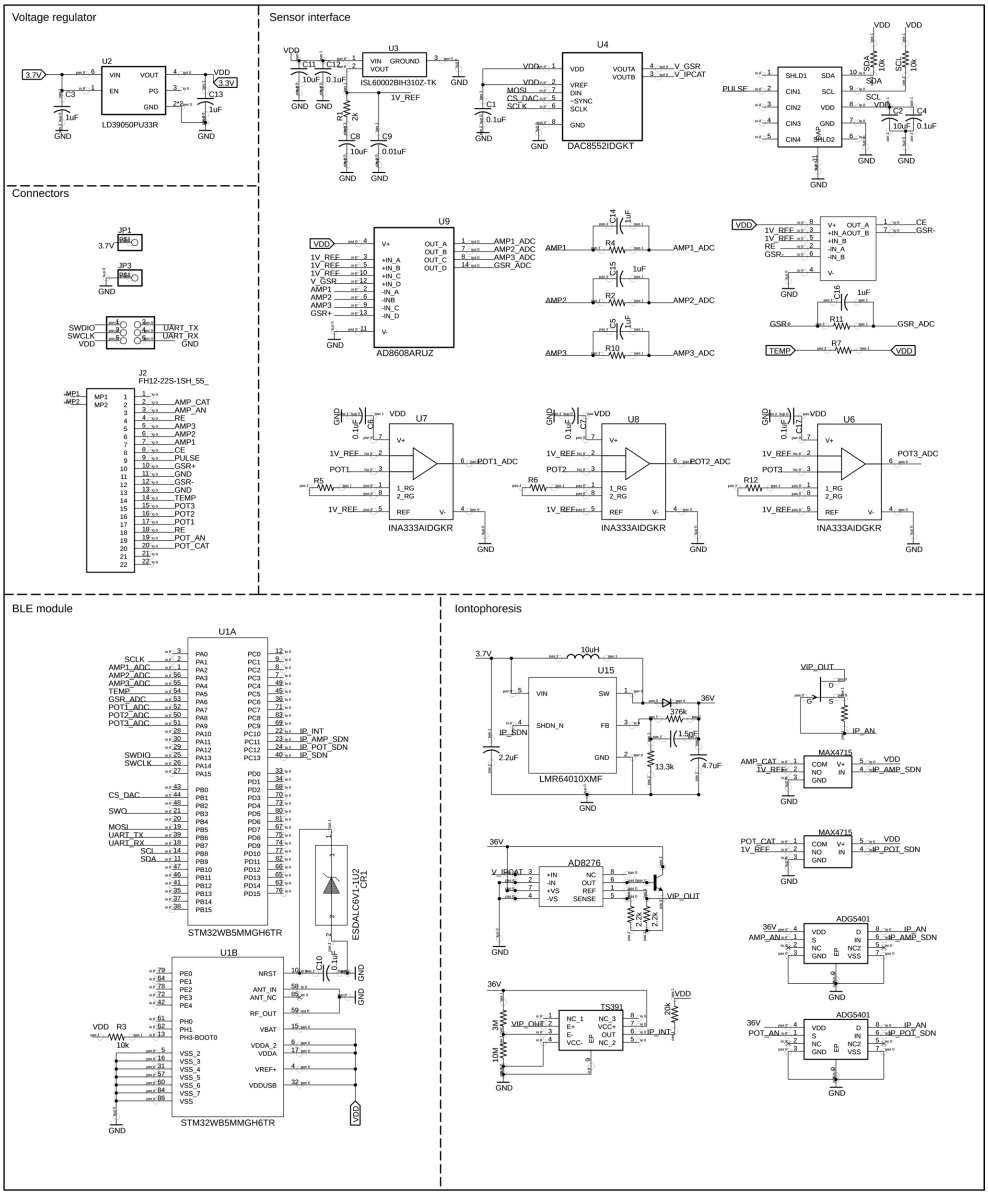

Supplementary Fig. 43 | Circuit schematic of the wireless wearable electronic system of the CARES.

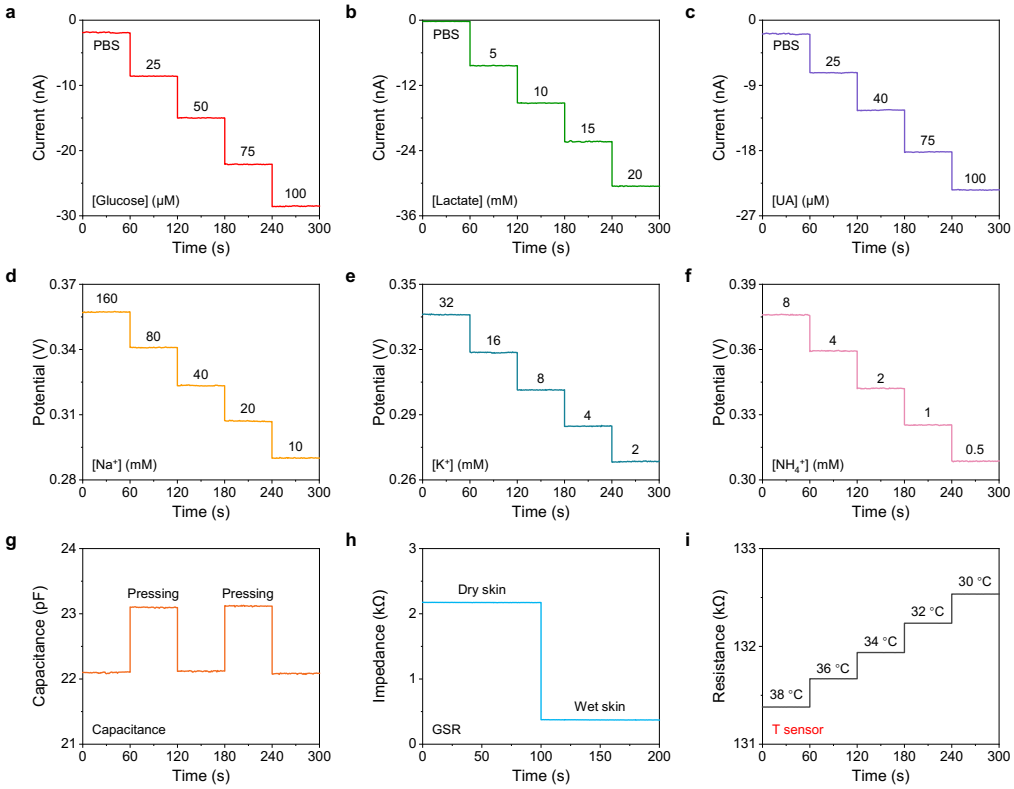

Supplementary Fig. 44 | In vitro sensor calibration and evaluation using the wireless wearable CARES system.

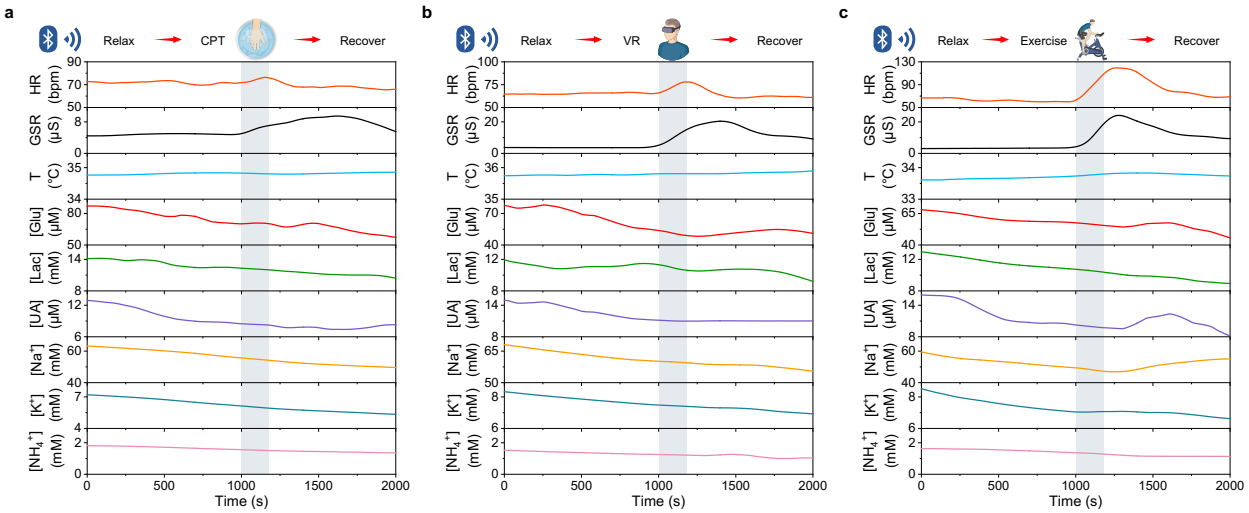

Supplementary Fig. 45 | Continuous data collection using the fully integrated wireless wearable CARES patch in laboratory conditions.

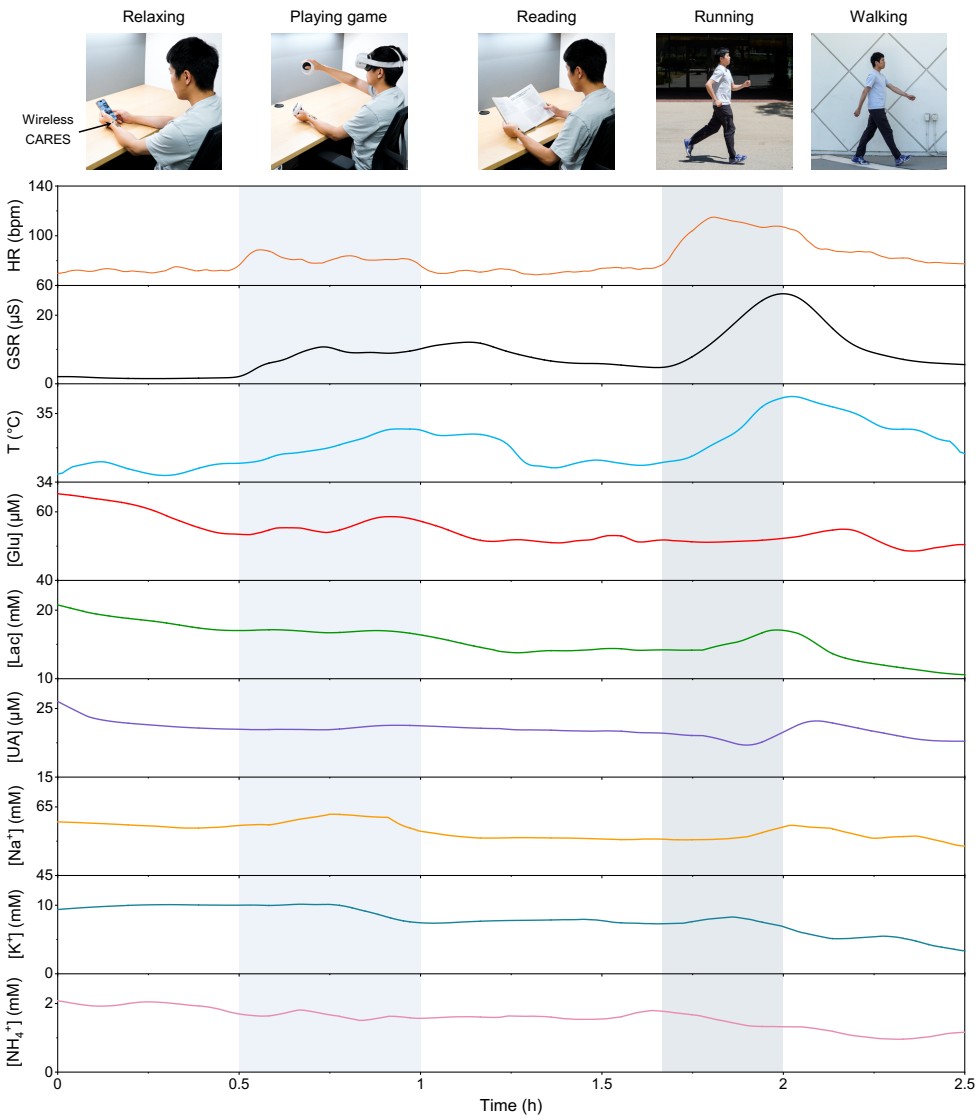

Supplementary Fig. 46 | Continuous data collection using the fully integrated wireless wearable CARES patch in real-life conditions.

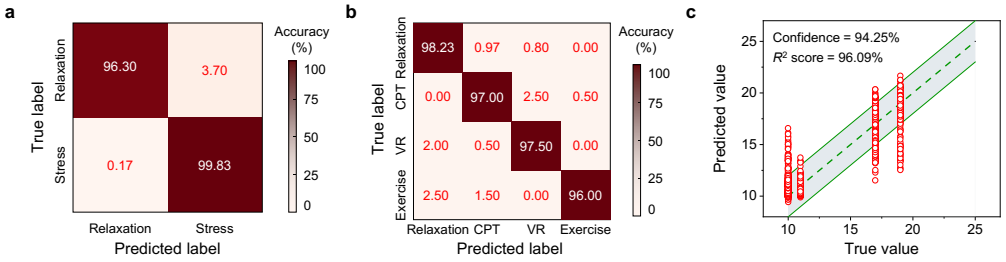

Supplementary Fig. 47 | ML-enabled stress response assessment based on the new datasets collected with wireless CARES patch in the laboratory setting. a, Confusion matrix displaying the classification accuracy for predicting stress and relaxation. **b**, Confusion matrix displaying the classification accuracy for predicting each type of stressor. **c,** True versus the ML-predicted state anxiety scores. Data is presented as ±2 state anxiety score buffer based on the potential error in the anxiety questionnaires.

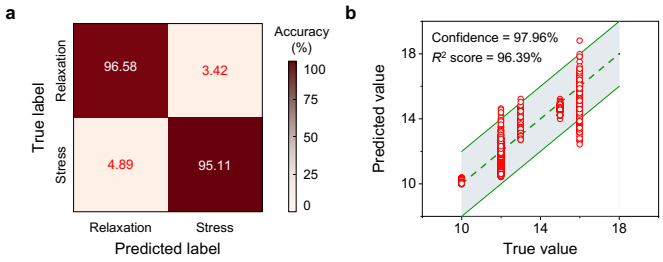

Supplementary Fig. 48 | Training and testing generalization of ML model for stress response assessment based on the new dataset collected by the wireless CARES in real-life settings. a, Confusion matrix displaying the classification accuracy for predicting stress and relaxation. **b**, True versus the ML-predicted state anxiety scores. Data is presented as ±2 state anxiety score buffer based on the potential error in the anxiety questionnaires.

Supplementary References

1. Epel, E. S. *et al.* More than a feeling: A unified view of stress measurement for population science. *Front. Neuroendocrinol.* **49**, 146–169 (2018).
2. Kagan, J. An Overly Permissive Extension. *Perspect. Psychol. Sci.* **11**, 442–450 (2016).
3. Richard S. Lazarus & Susan Folkman. *Stress, Appraisal, and Coping*. (Springer Publishing Company, 1984).
4. Endler, N. S. & Kocovski, N. L. State and trait anxiety revisited. *J. Anxiety Disord.* **15**, 231–245 (2001).
5. Fink, G. Chapter 1 - Stress, Definitions, Mechanisms, and Effects Outlined: Lessons from Anxiety. in *Stress: Concepts, Cognition, Emotion, and Behavior* 3–11 (Academic Press, 2016).
6. Cohen, S., Janicki-Deverts, D. & Miller, G. E. Psychological Stress and Disease. *JAMA* **298**, 1685–1687 (2007).
7. Friedman, E. S., Clark, D. B. & Gershon, S. Stress, anxiety, and depression: Review of biological, diagnostic, and nosologic issues. *J. Anxiety Disord.* **6**, 337–363 (1992).
8. Mental disorders. https://www.who.int/news-room/fact-sheets/detail/mental-disorders.
9. Craske, M. G. *et al.* Anxiety disorders. *Nat. Rev. Dis. Primers* **3**, 1–19 (2017).
10. *Diagnostic and statistical manual of mental disorders: DSM-5™, 5th ed*. (American Psychiatric Publishing, Inc., 2013).
11. Charmandari, E., Tsigos, C. & Chrousos, G. Endocrinology of the Stress Response. *Annu. Rev. Physiol.* **67**, 259–284 (2005).
12. Dolan, R. J. Emotion, Cognition, and Behavior. *Science* **298**, 1191–1194 (2002).
13. Harker, M. Psychological Sweating: A Systematic Review Focused on Aetiology and Cutaneous Response. *Skin Pharmacol. Physiol.* **26**, 92–100 (2013).
14. Sam, C. & Bordoni, B. Physiology, Acetylcholine. in *StatPearls* (StatPearls Publishing, 2023).
15. Gordan, R., Gwathmey, J. K. & Xie, L.-H. Autonomic and endocrine control of cardiovascular function. *World J. Cardiol.* **7**, 204–214 (2015).
16. Boucsein, W. *Electrodermal Activity*. (Springer Science & Business Media, 2012).
17. Kim, H. *et al.* Fully Integrated, Stretchable, Wireless Skin-Conformal Bioelectronics for Continuous Stress Monitoring in Daily Life. *Adv. Sci.* **7**, 2000810 (2020).
18. Kim, H. *et al.* Wireless, continuous monitoring of daily stress and management practice via soft bioelectronics. *Biosens. Bioelectron.* **173**, 112764 (2021).
19. Morales-López, C. A. Clinical relevance of stress biomarkers as health-disease indicators. *Mex. J. Med. Res.* **10**, 34–43 (2022).
20. Oka, T. Psychogenic fever: how psychological stress affects body temperature in the clinical population. *Temperature* **2**, 368–378 (2015).
21. Keum, Y. S., Kim, J.-H. & Li, Q. X. Biomarkers and Metabolomics, Evidence of Stress. in *Encyclopedia of Sustainability Science and Technology* 1184–1198 (Springer, 2012).
22. Noushad, S. *et al.* Physiological biomarkers of chronic stress: A systematic review. *Int. J. Health Sci.* **15**, 46–59 (2021).
23. Sharma, K. *et al.* Stress-Induced Diabetes: A Review. *Cureus* **14**, (2022).

24. Marcovecchio, M. L. & Chiarelli, F. The Effects of Acute and Chronic Stress on Diabetes Control. *Sci. Signal.* **5**, pt10 (2012).
25. Surwit, R. S., Schneider, M. S. & Feinglos, M. N. Stress and Diabetes Mellitus. *Diabetes Care* **15**, 1413–1422 (1992).
26. Sancini, A. & Tomei, F. Work related stress and blood glucose levels. *Ann. Ig.* **29**, 123–133 (2017).
27. Sim, Y.-B. *et al.* The regulation of blood glucose level in physical and emotional stress models: Possible involvement of adrenergic and glucocorticoid systems. *Arch. Pharm. Res.* **33**, 1679–1683 (2010).
28. Teague, C. R. *et al.* Metabonomic Studies on the Physiological Effects of Acute and Chronic Psychological Stress in Sprague−Dawley Rats. *J. Proteome Res.* **6**, 2080–2093 (2007).
29. Derbyshire, P. J., Barr, H., Davis, F. & Higson, S. P. J. Lactate in human sweat: a critical review of research to the present day. *J. Physiol. Sci.* **62**, 429–440 (2012).
30. Coco, M. *et al.* Influences of Blood Lactate Levels on Cognitive Domains and Physical Health during a Sports Stress. Brief Review. *Int. J. Environ. Res. Public Health.* **17**, 9043 (2020).
31. Proia, P., Di Liegro, C. M., Schiera, G., Fricano, A. & Di Liegro, I. Lactate as a Metabolite and a Regulator in the Central Nervous System. *Int. J. Mol. Sci.* **17**, 1450 (2016).
32. Hermann, R., Lay, D., Wahl, P., Roth, W. T. & Petrowski, K. Effects of psychosocial and physical stress on lactate and anxiety levels. *Stress* **22**, 664–669 (2019).
33. Kubera, B. *et al.* Rise in Plasma Lactate Concentrations with Psychosocial Stress: A Possible Sign of Cerebral Energy Demand. *OFA* **5**, 384–392 (2012).
34. Hall, J. B. & Brown, D. A. Plasma glucose and lactic acid alterations in response to a stressful exam. *Biol. Psychol.* **8**, 179–188 (1979).
35. Goodman, A. M. *et al.* The hippocampal response to psychosocial stress varies with salivary uric acid level. *Neuroscience* **339**, 396–401 (2016).
36. Rahe, R. H., Rubin, R. T. & Arthur, R. J. The Three Investigators Study. Serum Uric Acid, Cholesterol, and Cortisol Variability During Stresses of Everyday Life. *Psychosom. Med.* **36**, 258 (1974).
37. de Oliveira, L. F. G. *et al.* Uric Acid and Cortisol Levels in Plasma Correlate with Pre-Competition Anxiety in Novice Athletes of Combat Sports. *Brain Sci.* **12**, 712 (2022).
38. Melamed, S., Kushnir, T. & Shirom, A. Burnout and Risk Factors for Cardiovascular Diseases. *Behav. Med.* **18**, 53–60 (1992).
39. Albert, U. *et al.* Increased uric acid levels in bipolar disorder subjects during different phases of illness. *J. Affect. Disord.* **173**, 170–175 (2015).
40. Kesebir, S., Tatlıdil Yaylacı, E., Süner, Ö. & Gültekin, B. K. Uric acid levels may be a biological marker for the differentiation of unipolar and bipolar disorder: The role of affective temperament. *J. Affect. Disord.* **165**, 131–134 (2014).
41. Jahangard, L. *et al.* In a double-blind, randomized and placebo-controlled trial, adjuvant allopurinol improved symptoms of mania in in-patients suffering from bipolar disorder. *Eur. Neuropsychopharmacol.* **24**, 1210–1221 (2014).

42. Takahashi, H., Yoshika, M., Komiyama, Y. & Nishimura, M. The central mechanism underlying hypertension: a review of the roles of sodium ions, epithelial sodium channels, the renin–angiotensin–aldosterone system, oxidative stress and endogenous digitalis in the brain. *Hypertens. Res.* **34**, 1147–1160 (2011).
43. Krause, E. G. *et al.* Hydration State Controls Stress Responsiveness and Social Behavior. *J. Neurosci.* **31**, 5470–5476 (2011).
44. Cazalé, A. *et al.* Physiological stress monitoring using sodium ion potentiometric microsensors for sweat analysis. *Sens. Actuators B Chem.* **225**, 1–9 (2016).
45. Dong, M. *et al.* The stress, salt excretion, and nighttime blood pressure (SABRE) study: Rationale and study design. *Am. Heart J. Plus: Cardiol. Res. Pract.* **13**, 100099 (2022).
46. Ge, D. *et al.* Stress-Induced Sodium Excretion. *Hypertension* **53**, 262–269 (2009).
47. Clausen, T. Na+-K+ Pump Regulation and Skeletal Muscle Contractility. *Physiol. Rev.* **83**, 1269–1324 (2003).
48. Reid, J. L., Whyte, K. F. & Struthers, A. D. Epinephrine-induced hypokalemia: The role of beta adrenoceptors. *Am. J. Card.* **57**, F23–F27 (1986).
49. Dhama, K. *et al.* Biomarkers in Stress Related Diseases/Disorders: Diagnostic, Prognostic, and Therapeutic Values. *Front. Mol. Biosci.* **6**, 91 (2019).
50. O'Brien, P. D., Hinder, L. M., Callaghan, B. C. & Feldman, E. L. Neurological consequences of obesity. *Lancet Neurol.* **16**, 465–477 (2017).
51. Marshall, G. D. The Adverse Effects of Psychological Stress on Immunoregulatory Balance: Applications to Human Inflammatory Diseases. *Immunol. Allergy Clin. N. Am.* **31**, 133–140 (2011).
52. Gianaros, P. J. & Jennings, J. R. Host in the Machine: A Neurobiological Perspective on Psychological Stress and Cardiovascular Disease. *Am. Psychol.* **73**, 1031–1044 (2018).
53. Hughes-Austin, J. M. *et al.* The Relation of Serum Potassium Concentration with Cardiovascular Events and Mortality in Community-Living Individuals. *Clin. J. Am. Soc. Nephrol.* **12**, 245 (2017).
54. Sica, D. A. *et al.* Importance of Potassium in Cardiovascular Disease. *J. Clin. Hypertens.* **4**, 198–206 (2002).
55. Sato, K., Kang, W. H., Saga, K. & Sato, K. T. Biology of sweat glands and their disorders. I. Normal sweat gland function. *J. Am. Acad. Dermatol.* **20**, 537–563 (1989).
56. Vere, C. C., Streba, C. T., Streba, L. M., Ionescu, A. G. & Sima, F. Psychosocial stress and liver disease status. *World J. Gastroenterol.* **15**, 2980–2986 (2009).
57. Guinovart, T., J. Bandodkar, A., R. Windmiller, J., J. Andrade, F. & Wang, J. A potentiometric tattoo sensor for monitoring ammonium in sweat. *Analyst* **138**, 7031–7038 (2013).
58. Buono, M. J., Clancy, T. R. & Cook, J. R. Blood lactate and ammonium ion accumulation during graded exercise in humans. *J. Appl. Physiol.* **57**, 135–139 (1984).
59. Noël, J.-M., Médard, J., Combellas, C. & Kanoufi, F. Prussian Blue Degradation during Hydrogen Peroxide Reduction: A Scanning Electrochemical Microscopy Study on the Role of the Hydroxide Ion and Hydroxyl Radical. *ChemElectroChem* **3**, 1178–1184 (2016).

60. Karyakin, A. A. Prussian Blue and Its Analogues: Electrochemistry and Analytical Applications. *Electroanalysis* **13**, 813–819 (2001).
61. Fu, H. *et al.* Enhanced storage of sodium ions in Prussian blue cathode material through nickel doping. *J. Mater. Chem. A* **5**, 9604–9610 (2017).
62. Xu, C. *et al.* Prussian Blue Analogues in Aqueous Batteries and Desalination Batteries. *Nano-Micro Lett.* **13**, 166 (2021).
63. Hurlbutt, K., Wheeler, S., Capone, I. & Pasta, M. Prussian Blue Analogs as Battery Materials. *Joule* **2**, 1950–1960 (2018).
64. You, Y., Wu, X.-L., Yin, Y.-X. & Guo, Y.-G. A zero-strain insertion cathode material of nickel ferricyanide for sodium-ion batteries. *J. Mater. Chem. A* **1**, 14061–14065 (2013).
65. Shao, Y., Ying, Y. & Ping, J. Recent advances in solid-contact ion-selective electrodes: functional materials, transduction mechanisms, and development trends. *Chem. Soc. Rev.* **49**, 4405–4465 (2020).
66. Armas, S. Development and Characterization of Solid-Contact Paper-Based and Micro Ion-Selective Electrodes for Environmental Analysis. *Electronic Theses and Dissertations, 2004-2019* (2018).
67. Gao, W. *et al.* Fully integrated wearable sensor arrays for multiplexed *in situ* perspiration analysis. *Nature* **529**, 509–514 (2016).
68. Joon, N. K., He, N., Ruzgas, T., Bobacka, J. & Lisak, G. PVC-Based Ion-Selective Electrodes with a Silicone Rubber Outer Coating with Improved Analytical Performance. *Anal. Chem.* **91**, 10524–10531 (2019).
69. Le Floch, P. *et al.* Fundamental Limits to the Electrochemical Impedance Stability of Dielectric Elastomers in Bioelectronics. *Nano Lett.* **20**, 224–233 (2020).
70. *A Handbook for the Study of Mental Health: Social Contexts, Theories, and Systems*. (Cambridge University Press, 2009). doi:10.1017/CBO9780511984945.
71. Elizabeth L. Hay & Manfred Diehl. Reactivity to daily stressors in adulthood: The importance of stressor type in characterizing risk factors. *Psychol. Aging* **25**, 118–131 (2010).
72. Pow, J., Lee-Baggley, D. & DeLongis, A. Threats to communion and agency mediate associations between stressor type and daily coping. *Anxiety, Stress, & Coping* **29**, 660–672 (2016).
73. Stern, M., Norman, S. & Komm, C. Medical Students' Differential Use of Coping Strategies as a Function of Stressor Type, Year of Training, and Gender. *Behav. Med.* **18**, 173–180 (1993).
74. Vedhara, K., Shanks, N., Anderson, S. & Lightman, S. The Role of Stressors and Psychosocial Variables in the Stress Process: A Study of Chronic Caregiver Stress. *Psychosom. Med.* **62**, 374 (2000).
75. Lin, M. & Ling, Q. Is role stress always harmful? Differentiating role overload and role ambiguity in the challenge-hindrance stressors framework. *Tour. Manag.* **68**, 355–366 (2018).
76. Compas, B. E. Coping with stress during childhood and adolescence. *Psychol. Bull.* **101**, 393–403 (1987).

77. Wenz-Gross, M., Siperstein, G. N., Untch, A. S. & Widaman, K. F. Stress, Social Support, and Adjustment of Adolescents in Middle School. *J. Early Adolesc.* **17**, 129–151 (1997).
78. Stern, M. & Zevon, M. A. Stress, Coping, and Family Environment: The Adolescent's Response to Naturally Occurring Stressors. *J. Adolesc. Res.* **5**, 290–305 (1990).
79. Pohl, J., Olmstead, M. C., Wynne-Edwards, K. E., Harkness, K. & Menard, J. L. Repeated exposure to stress across the childhood-adolescent period alters rats' anxiety- and depression-like behaviors in adulthood: The importance of stressor type and gender. *Behav. Neurosci.* **121**, 462–474 (2007).
80. Pallavicini, F., Argenton, L., Toniazzi, N., Aceti, L. & Mantovani, F. Virtual Reality Applications for Stress Management Training in the Military. *Aerosp. Med. Hum. Perform.* **87**, 1021–1030 (2016).
81. Miyahira, S. D., Folen, R. A., Hoffman, H. G., Garcia-Palacios, A. & Schaper, K. M. Effectiveness of brief VR treatment for PTSD in war-fighters: a case study. *Stud. Health Technol. Inform.* **154**, 214–219 (2010).
82. Crestani, C. C. Emotional Stress and Cardiovascular Complications in Animal Models: A Review of the Influence of Stress Type. *Front. Physiol.* **7**, (2016).
83. Can, Y. S. *et al.* Personal Stress-Level Clustering and Decision-Level Smoothing to Enhance the Performance of Ambulatory Stress Detection With Smartwatches. *IEEE Access* **8**, 38146–38163 (2020).
84. Oken, B. S., Chamine, I. & Wakeland, W. A systems approach to stress, stressors and resilience in humans. *Behav. Brain Res.* **282**, 144–154 (2015).
85. Schwabe, L., Haddad, L. & Schachinger, H. HPA axis activation by a socially evaluated cold-pressor test. *Psychoneuroendocrinology* **33**, 890–895 (2008).
86. Torrente-Rodríguez, R. M. *et al.* Investigation of Cortisol Dynamics in Human Sweat Using a Graphene-Based Wireless mHealth System. *Matter* **2**, 921–937 (2020).
87. Zhao, Q. *et al.* Reproducibility of Blood Pressure Response to the Cold Pressor Test: The GenSalt Study. *Am. J. Epidemiol.* **176**, S91–S98 (2012).
88. Ward, M. M. *et al.* Epinephrine and Norepinephrine Responses in Continuously Collected Human Plasma to a Series of Stressors. *Psychosom. Med.* **45**, 471 (1983).
89. Fadeev, K. A. *et al.* Too Real to Be Virtual: Autonomic and EEG Responses to Extreme Stress Scenarios in Virtual Reality. *Behav. Neurol.* **2020**, e5758038 (2020).
90. Ahmad, Z. *et al.* Multi-Level Stress Assessment from ECG in a Virtual Reality Environment Using Multimodal Fusion. Preprint at https://arxiv.org/abs/2107.04566 (2022).
91. Meehan, M., Insko, B., Whitton, M. & Brooks, F. P. Physiological measures of presence in stressful virtual environments. *ACM Trans. Graph.* **21**, 645–652 (2002).
92. Martens, M. A. *et al.* It feels real: physiological responses to a stressful virtual reality environment and its impact on working memory: *J. Clin. Psychopharmacol.* **33**, 1264–1273 (2019).
93. Pallavicini, F. *et al.* Interreality for the management and training of psychological stress: study protocol for a randomized controlled trial. *Trials* **14**, 191 (2013).

94. Pallavicini, F., Pepe, A. & Minissi, M. E. Gaming in Virtual Reality: What Changes in Terms of Usability, Emotional Response and Sense of Presence Compared to Non-Immersive Video Games? *Simul. Gaming* **50**, 136–159 (2019).
95. Pallavicini, F. & Pepe, A. Comparing Player Experience in Video Games Played in Virtual Reality or on Desktop Displays: Immersion, Flow, and Positive Emotions. in *CHI PLAY'19* 195–210 (Association for Computing Machinery, 2019).
96. Nunes, M. J., Cordas, C. M., Moura, J. J. G., Noronha, J. P. & Branco, L. C. Screening of Potential Stress Biomarkers in Sweat Associated with Sports Training. *Sports Med. Open* **7**, 8 (2021).
97. Fortunato, A. K. *et al.* Strength Training Session Induces Important Changes on Physiological, Immunological, and Inflammatory Biomarkers. *J. Immunol. Res.* **2018**, e9675216 (2018).
98. Wielemborek-Musial, K., Szmigielska, K., Leszczynska, J. & Jegier, A. Blood Pressure Response to Submaximal Exercise Test in Adults. *BioMed Res. Int.* **2016**, e5607507 (2016).
99. Sharman, J. E. & LaGerche, A. Exercise blood pressure: clinical relevance and correct measurement. *J. Hum. Hypertens.* **29**, 351–358 (2015).
100. Kurl, S. *et al.* Systolic Blood Pressure Response to Exercise Stress Test and Risk of Stroke. *Stroke* **32**, 2036–2041 (2001).
101. Franz, I. W. Blood pressure measurement during ergometric stress testing. *Z. Kardiol.* **85 Suppl 3**, 71–75 (1996).
102. Pa, H. Exercise stress testing in blood pressure evaluation. *J. Am. Board Fam. Prac.* **2**, (1989).
103. Klous, L., de Ruiter, C. J., Scherrer, S., Gerrett, N. & Daanen, H. A. M. The (in)dependency of blood and sweat sodium, chloride, potassium, ammonia, lactate and glucose concentrations during submaximal exercise. *Eur. J. Appl. Physiol.* **121**, 803–816 (2021).
104. Cohen, S., Kamarck, T. & Mermelstein, R. A Global Measure of Perceived Stress. *J. Health Soc. Behav.* **24**, 385–396 (1983).
105. Levenstein, S. *et al.* Development of the perceived stress questionnaire: A new tool for psychosomatic research. *J. Psychosom. Res.* **37**, 19–32 (1993).
106. Lovibond, S. H. & Lovibond, P. F. Manual for the depression anxiety stress scales. *Psychology Foundation of Australia* (1995).
107. Spielberger, C. Manual for the State-Trait Anxiety Inventory (STAI Form Y). *Consulting Psychologists Press, Inc.* (1983).
108. Birkett, M. A. The Trier Social Stress Test Protocol for Inducing Psychological Stress. *J. Vis. Exp.* **56**, e3238 (2011).
109. Schmidt, P., Reiss, A., Duerichen, R., Marberger, C. & Van Laerhoven, K. Introducing WESAD, a Multimodal Dataset for Wearable Stress and Affect Detection. in *ICMI '18* 400–408 (2018).
110. Gjoreski, M., Gjoreski, H., Luštrek, M. & Gams, M. Continuous Stress Detection Using a Wrist Device: In Laboratory and Real Life. in *UbiComp '16* 1185–1193 (2016).

111. Gjoreski, M., Luštrek, M., Gams, M. & Gjoreski, H. Monitoring stress with a wrist device using context. *J. Biomed. Inform.* **73**, 159–170 (2017).
112. Ahmad, Z. & Khan, N. M. Multi-level Stress Assessment Using Multi-domain Fusion of ECG Signal. in *EMBC* 4518–4521 (2020).
113. Beck, A. T., Epstein, N., Brown, G. & Steer, R. A. An inventory for measuring clinical anxiety: psychometric properties. *J. Consult. Clin. Psychol.* **56**, 893–897 (1988).
114. Zigmond, A. S. & Snaith, R. P. The hospital anxiety and depression scale. *Acta Psychiatr. Scand.* **67**, 361–370 (1983).
115. Ghassemi, M., Oakden-Rayner, L. & Beam, A. L. The false hope of current approaches to explainable artificial intelligence in health care. *The Lancet Digital Health* **3**, e745–e750 (2021).
116. The Dark Secret at the Heart of AI. *MIT Technology Review* https://www.technologyreview.com/2017/04/11/5113/the-dark-secret-at-the-heart-of-ai/.
117. Lundberg, S. M. & Lee, S.-I. A Unified Approach to Interpreting Model Predictions. in *Advances in Neural Information Processing Systems* vol. 30 (Curran Associates, Inc., 2017).
118. Lin, Y. *et al.* Porous Enzymatic Membrane for Nanotextured Glucose Sweat Sensors with High Stability toward Reliable Noninvasive Health Monitoring. *Adv. Funct. Mater.* **29**, 1902521 (2019).
119. Lee, H. *et al.* A graphene-based electrochemical device with thermoresponsive microneedles for diabetes monitoring and therapy. *Nat. Nanotechnol.* **11**, 566–572 (2016).
120. Koh, A. *et al.* A soft, wearable microfluidic device for the capture, storage, and colorimetric sensing of sweat. *Sci. Transl. Med.* **8**, 366ra165-366ra165 (2016).
121. Martín, A. *et al.* Epidermal Microfluidic Electrochemical Detection System: Enhanced Sweat Sampling and Metabolite Detection. *ACS Sens.* **2**, 1860–1868 (2017).
122. Munje, R. D., Muthukumar, S. & Prasad, S. Lancet-free and label-free diagnostics of glucose in sweat using Zinc Oxide based flexible bioelectronics. *Sens. Actuators B Chem.* **238**, 482–490 (2017).
123. Jia, W. *et al.* Electrochemical Tattoo Biosensors for Real-Time Noninvasive Lactate Monitoring in Human Perspiration. *Anal. Chem.* **85**, 6553–6560 (2013).
124. Sempionatto, J. R. *et al.* Eyeglasses based wireless electrolyte and metabolite sensor platform. *Lab Chip* **17**, 1834–1842 (2017).
125. Yang, Y. *et al.* A laser-engraved wearable sensor for sensitive detection of uric acid and tyrosine in sweat. *Nat. Biotechnol.* **38**, 217–224 (2020).
126. Bandodkar, A. J. *et al.* Epidermal tattoo potentiometric sodium sensors with wireless signal transduction for continuous non-invasive sweat monitoring. *Biosens. Bioelectron.* **54**, 603–609 (2014).
127. Cheong, Y. H., Ge, L., Zhao, N., Teh, L. K. & Lisak, G. Ion selective electrodes utilizing a ferrocyanide doped redox active screen-printed solid contact - impact of electrode response to conditioning. *J. Electroanal. Chem.* **870**, 114262 (2020).

128. Rius-Ruiz, F. X. *et al.* Potentiometric Strip Cell Based on Carbon Nanotubes as Transducer Layer: Toward Low-Cost Decentralized Measurements. *Anal. Chem.* **83**, 8810–8815 (2011).
129. Wang, S. *et al.* Wearable Sweatband Sensor Platform Based on Gold Nanodendrite Array as Efficient Solid Contact of Ion-Selective Electrode. *Anal. Chem.* **89**, 10224–10231 (2017).
130. Ping, J. *et al.* High-performance flexible potentiometric sensing devices using free-standing graphene paper. *J. Mater. Chem. B* **1**, 4781–4791 (2013).
131. Klink, S., Ishige, Y. & Schuhmann, W. Prussian Blue Analogues: A Versatile Framework for Solid-Contact Ion-Selective Electrodes with Tunable Potentials. *ChemElectroChem* **4**, 490–494 (2017).
132. Rigas, G., Goletsis, Y. & Fotiadis, D. I. Real-Time Driver's Stress Event Detection. *IEEE Trans. Intell. Transp. Syst.* **13**, 221–234 (2012).
133. Hwang, B. *et al.* Deep ECGNet: An Optimal Deep Learning Framework for Monitoring Mental Stress Using Ultra Short-Term ECG Signals. *Telemed. e-Health* **24**, 753–772 (2018).
134. Saeed, A., Ozcelebi, T., Lukkien, J., van Erp, J. B. F. & Trajanovski, S. Model Adaptation and Personalization for Physiological Stress Detection. in *2018 IEEE 5th International Conference on Data Science and Advanced Analytics (DSAA)* 209–216 (2018). doi:10.1109/DSAA.2018.00031.
135. Hernandez, J., Morris, R. R. & Picard, R. W. Call Center Stress Recognition with Person-Specific Models. in *Affective Computing and Intelligent Interaction* (eds. D'Mello, S., Graesser, A., Schuller, B. & Martin, J.-C.) 125–134 (Springer, 2011). doi:10.1007/978-3-642-24600-5_16.
136. Choi, J., Ahmed, B. & Gutierrez-Osuna, R. Development and Evaluation of an Ambulatory Stress Monitor Based on Wearable Sensors. *IEEE Trans. Inf. Technol. Biomed.* **16**, 279–286 (2012).
137. Zubair, M., Yoon, C., Kim, H., Kim, J. & Kim, J. Smart Wearable Band for Stress Detection. in *2015 5th International Conference on IT Convergence and Security (ICITCS)* 1–4 (2015). doi:10.1109/ICITCS.2015.7293017.
138. Healey, J. A. & Picard, R. W. Detecting stress during real-world driving tasks using physiological sensors. *IEEE Trans. Intell. Transp. Syst.* **6**, 156–166 (2005).